UNIVERSIDAD TECNICA
FEDERICO SANTA MARIA

Departamento de Obras Civiles

WAVE-RIVER INTERACTIONS AT A SMALL SCALE RIVER MOUTH: FIELD OBSERVATIONS AT THE MAIPO RIVER, CENTRAL CHILE

Thesis submitted by:

Alonso Andrés Roco Fuentes

in fulfillment of the requirements for the degree of

Civil Engineer

and the degree of

Master of Science in Civil Engineering

Advisor
Raúl Flores Audibert

JUNE, 2023

UNIVERSIDAD TECNICA
FEDERICO SANTA MARIA

THESIS TITLE:

WAVE-RIVER INTERACTIONS AT A SMALL SCALE RIVER MOUTH: FIELD OBSERVATIONS AT THE MAIPO RIVER, CENTRAL CHILE

AUTHOR:

Alonso Andrés Roco Fuentes

A thesis submitted to the Federico Santa María Technical University in fulfilment of the requirements for the degree of Civil Engineer and the degree of Master of Science in Civil Engineering.

PhD Raúl Flores Audibert: .....

PhD Megan Elizabeth Williams: .....

PhD Patricio Catalán Mondaca: .....

Valparaíso, Chile, Friday 30th June, 2023

(...) dedicatoria

Agradecimientos

Abstract

Small coastal rivers often discharge directly into the surfzone, where the fate of freshwater and river-borne materials (e.g., sediment, nutrients and contaminants) is primarily determined by the combined effects of buoyant plume processes and the nearshore wave forcing. Understanding river-wave interactions in the surfzone is essential to assess coastal water quality and impacts on ecosystem health along adjacent shorelines. These interactions are modulated by the variability in river discharge, offshore wave climate, tidal forcing and surfzone dynamics, and therefore occur over a wide range of timescales. However, the different time scales at which river-wave interactions occur have not been fully investigated. In this work we use *in situ* and remote (drone-based) observations collected at the mouth of the Maipo River —a small-scale river system in central Chile— to investigate the interactions between the river outflow and the incident wave forcing that may influence the distribution of freshwater along the coast. We focus on interactions occurring at infragravity (wave groups), tidal, and synoptic (offshore wave climate) timescales. The observations included inlet and surfzone deployments, and documented low river discharge conditions ($Q_R \sim 20 - 27\ [m^3/s]$) and variable wave forcing ($H_s \sim 1 - 3\ [m]$). We observed that the salinity signal at the river mouth is strongly modulated by the tide, with a freshwater plume forming solely during the ebb. Large oscillations associated to infragravity (IG) motions are continuously observed on top of the tidal variability. These oscillations are evidenced in surfzone salinity, inlet water levels and inlet velocity during the early ebb when the freshwater plume starts to develop. As the plume evolves into a strong outflow jet during the late ebb, they are largely blocked from propagating into the inlet, being restricted to the surfzone. The combined analysis of drone imagery and *in situ* observations suggests that the surfzone salinity variability at IG frequencies is associated with the arrival of wave groups and the propagation of wave fronts in the plume area. In particular, we found that, during the late ebb, the large oscillations in surfzone salinity (amplitude of 15-20 psu) are explained by a contraction and expansion of the outflow plume in response to the variability in the onshore wave forcing at the timescale of wave groups. On synoptic timescales (hours to days), the surfzone salinity responded to the intensity of the offshore wave forcing ($\sim 20\ [m]$ depth), with higher waves promoting lower salinity as freshwater is mostly retained near the coast. A wave-river momentum balance confirms that the wave forcing had the potential to trap freshwater in the surfzone. This study shows that nearshore waves influence the final fate of freshwater and terrestrial materials on a wide range of timescales, from infragravity ($1 - 5\ [min]$) to hours and days.

Resumen

Los ríos costeros de pequeña escala a menudo descargan directamente en la zona de rompiente, donde el destino del agua dulce y los materiales transportados por los ríos (e.g., sedimentos, nutrientes y contaminantes) está determinado principalmente por los efectos combinados de los procesos de buoyancia de la pluma y el forzante de oleaje costero. Comprender la interacción río-oleaje en la zona rompiente es esencial para evaluar la calidad del agua y los impactos sobre los ecosistemas en las zonas costeras aledañas. Estas interacciones están moduladas por la variabilidad en el caudal del río, el clima de oleaje en aguas profundas, el forzante de marea, y la dinámica de la zona rompiente. Sin embargo, las diferentes escalas de tiempo en que la interacción río-oleaje ocurre no han sido investigadas a cabalidad. En este trabajo utilizamos observaciones *in situ* y remotas (basadas en drones) recolectadas en la desembocadura del río Maipo —un sistema fluvial de pequeña escala en Chile central— para investigar la interacción entre la descarga del río y el forzante del oleaje incidente, la cual puede influir en la distribución de agua dulce a lo largo de la costa. Nos enfocamos en interacciones que ocurren en escalas de tiempo de infragravedad (grupos de oleaje), mareal, y sinóptica (clima de oleaje en aguas profundas). Las observaciones incluyeron mediciones en el estuario y zona de rompiente; y registraron bajo caudal de descarga ($Q_R \sim 20 - 27\ [m^3/s]$) y clima de oleaje variable ($H_s \sim 1 - 3\ [m]$). Observamos que la señal de salinidad en la desembocadura del río está fuertemente modulada por la marea, con una pluma formándose únicamente durante la fase vaciante. Se observan continuamente grandes oscilaciones asociadas a infragravedad (IG) además de la variabilidad de las mareas. Estas oscilaciones se evidencian en la salinidad de la zona rompiente, el nivel de agua en el estuario, y la velocidad de la descarga; durante la primera mitad de la fase vaciante, cuando la pluma de agua dulce comienza a desarrollarse. A medida que la pluma se convierte en un fuerte *jet* de salida durante la segunda mitad de la fase vaciante, las oscilaciones son bloqueadas evitando así su propagación hacia el estuario, quedando restringidas a la zona rompiente. El análisis combinado de las imágenes de dron y las observaciones *in situ* sugieren que la variabilidad de la salinidad de la zona de rompiente en frecuencias de IG está asociada con la llegada de grupos de oleaje y la propagación de frentes de olas en la zona de la pluma. En particular, se encontró que durante la segunda mitad de la fase vaciante las grandes oscilaciones de salinidad de la zona de rompiente ($15 - 20\ [psu]$) se explican por una contracción y expansión de la pluma en respuesta a la variabilidad en el forzante de oleaje en la escala de tiempo de grupos. En escalas de tiempo sinópticas (horas a días), la salinidad de la zona rompiente responde a la intensidad del forzante de oleaje en aguas profundas ($\sim 20\ [m]$ de profundidad), con olas más altas provocando menor salinidad ya que el agua dulce se retiene principalmente cerca de la costa. Un balance de momentum entre la descarga del río y el forzante de oleaje confirma que éste último tiene potencial de atrapar agua dulce en la zona de rompiente. Este estudio muestra que el oleaje costero influye en el destino final del agua dulce y el material terrestre que ésta transporta en una amplia gama de escalas de tiempo, desde infragravedad ($1 - 5\ [min]$) hasta horas y días.

Contents

List of Figures

Chapter 1

Introduction

1.1 Motivation

Coastal zones are essential not only for ecological systems and processes, but for economical and social development (e.g., Costanza, 1999; Martínez et al., 2007; Poe et al., 2014; Littles et al., 2018). These environments hold a wide variety of biomes presenting unique rich biodiversity that is home to more than 1 million species already described considering all coastline different ecosystems (i.e., aquatic, inter-tidal and terrestrial) (Martínez et al., 2007), with an estimation of 10 million once all species have been found (Reid and Miller, 1989). In terms of economical relevance, coastal zones provide goods (e.g., food, salt, minerals, oils, construction materials) and services (e.g., shoreline protection against natural hazards, storing and cycling nutrients, sustaining biodiversity, water capture, recreation and tourism) highly valuable to society (Martínez et al., 2007). Furthermore, its social importance is clear when analysing population distribution in coastal regions. Although 72% of coastline can be considered natural (Burke et al., 2001), 53% of urban population (i.e., cities with ≥ 100000 inhabitants) live within $100[km]$ from the coast (Barragán and De Andrés, 2015); presenting much higher population density —nearly 3 times world's average density— (Small and Nicholls, 2003). This demographic phenomena is explained by the beauty of coastal ecosystems, its high accessibility and the numerous services it offers (Martínez et al., 2007). Urban centres located far away from the sea may also impact in the coastal environments, as rivers collect and transport material from watersheds and discharges into the sea.

Many coastal sites throughout the world are influenced by small-scale river mouths, which serve as the main conduit for the exchange of mass between watersheds and the coastal ocean (e.g., Farnsworth and Milliman, 2003). Studies have highlighted the important role of small rivers on freshwater, sediment and nutrient delivery to the world's coasts, with an estimated global contribution that is comparable to that of large river systems (Milliman and Syvitski, 1992; Syvitski et al., 2003; Farnsworth and Milliman, 2003; Izett and Fennel, 2018). The dispersal patterns of river-borne materials in small coastal rivers directly influence water quality, biogeochemical cycles, beach contamination and pollution dispersal, sediment budgets and morphodynamics along adjacent shorelines (e.g., Warrick and Milliman, 2003; Grant et al., 2005; Goñi et al., 2013; Masotti et al., 2018; Feddersen et al., 2021). Consequently, understanding the processes that determine the dispersal and mixing of river water in the nearshore is essential to develop efficient coastal management strategies, as well as for developing predictive capabilities to quantify the impact of anthropogenic interventions in coastal systems (e.g., Farnsworth and Milliman, 2003).

1.2 River Plumes Hydrodinamics

Similarly to large river discharges, the dynamics of small-scale coastal plumes have been shown to be influenced by tides (Pritchard and Huntley, 2006; Bricker et al., 2006; Basdurak et al., 2020; Flores et al., 2022) and winds (Warrick et al., 2007; Osadchiev et al., 2021; Basdurak and Largier, 2022). However, as small river systems often discharge directly into energetic surfzone regions, the nearshore wave forcing and wave-driven processes may strongly influence plume dynamics and may be expected to dominate the initial spreading and mixing processes (Wong et al., 2013; Delpey et al., 2014; Rodriguez et al., 2018; Kastner et al., 2019; Flores et al., 2022; Kastner et al., 2022). Small coastal plumes can be greatly modified in the surfzone due to wave processes such as wave-driven currents that result from gradients in the radiation stresses (e.g., Longuet-Higgins and Stewart, 1964) and wave breaking, which provides a considerable amount of turbulence at the surface (Feddersen, 2012), promotes freshwater mixing (Kastner et al., 2022) and exerts an onshore directed force (e.g., Feddersen et al., 2016; Moghimi et al., 2019).

Only recently these effects have started to be investigated, primarily based on numerical studies (e.g., Delpey et al., 2014; Rodriguez et al., 2018; Moghimi et al., 2019). Numerical studies on small-scale river mouths and tidal inlets show the potential for the wave forcing to prevent small plumes from expanding freely towards the ocean beyond the surfzone, as the momentum released by incoming waves can slow down the outgoing freshwater plume and confine it to the shoreline (Rodriguez et al., 2018; Moghimi et al., 2019). Results from these modeling studies indicate that the depth-limited breaking of short waves in the surfzone exerts a depth-integrated wave force that limits the cross-shore spreading of the plume and traps freshwater in the surfzone (e.g., Rodriguez et al., 2018; Moghimi et al., 2019), forcing the alongshore transport of terrestrial materials (e.g. Feddersen et al., 2016; Rodriguez et al., 2018). Model simulations also suggest that enhanced vertical mixing due to wave breaking results in a well-mixed surfzone or with very little vertical stratification (Rodriguez et al., 2018; Moghimi et al., 2019). The idealized numerical simulations by Rodriguez et al. (2018) showed that the percentage of freshwater that is retained in the surfzone is related to the ratio of river momentum flux and wave momentum flux (radiation stresses); large part of the freshwater input escapes the surfzone when river momentum exceeds the incident wave momentum, whereas most freshwater is entrained into the surfzone when the wave momentum dominates. Salinity data by Kastner et al. (2019) supports this framework, as freshwater events outside the surfzone were observed near local peaks of the river momentum-to-wave momentum ratio, usually occurring close to low water.

Field studies, although very scarce, have also reported surfzone trapped river plumes (e.g., Wong et al., 2013; Kastner et al., 2019; Flores et al., 2022). Conceptual models based on field measurements have been proposed to predict if river water is transported beyond the surfzone (e.g., Wong et al., 2013; Kastner et al., 2019). These models use length scales based on the river outflow momentum and the wave-driven momentum, which are compared to the surfzone width (L_{SZ}) to assess the potential for river water to escape the surfzone (Wong et al., 2013; Kastner et al., 2019). Wong et al. (2013) used a cross-flow length scale (L_a), determined by the discharge momentum and the wave-driven alongshore velocity (Jones et al., 2007; Wong et al., 2013), and proposed that if $L_{SZ}/L_a < 10$ river water exits the surfzone using measurements at the mouth of a small creek in California. A near-field plume length (L_{NF}) based on discharge momentum and plume buoyancy (e.g. Jones et al., 2007; Hetland, 2010) was used by Kastner et al. (2019) to describe plume escapes at the Quinault River, Oregon; they found that if $L_{NF}/L_{SZ} > 1$ the river water escapes the surfzone as discharge momentum overcomes the wave forcing. Kastner et al. (2022) used the same dataset to investigate plume mixing in the surfzone and concluded that observed mixing rates are primarily driven by changes in stratification, which result from tidal modulations in freshwater discharge and not the wave conditions. In light of those results,

the authors suggest that wave-breaking turbulence is sufficient to cause vertical mixing over all observed conditions (Kastner et al., 2022).

Recently, Flores et al. (2022) reported modulations of a surfzone trapped plume by infragravity (IG) wave forcing using field measurements at the mouth of the Maipo river (a small-scale river in central Chile). Infragravity waves are long surface ocean waves with frequencies that are usually defined between 0.004 and 0.04 Hz (e.g., Pomeroy et al., 2012; Bertin et al., 2018), and are mostly associated to the presence of groups in the incident short waves (Longuet-Higgins and Stewart, 1962; Symonds et al., 1982). The observations of Flores et al. (2022) showed persistent fluctuations in outflow river velocity, inlet water levels and surfzone salinity at IG wave periods (30-300 sec), and that cross-shore plume extent was also modulated at these periods in the surfzone. They reported the plume expanding and contracting by 20-50% at IG wave frequencies. The oscillations in plume width at IG frequencies were negatively correlated with the width of the surfzone, which is modulated by the arrival and depth-limited breaking of low and high amplitude waves (wave groups) (e.g. Symonds et al., 1982). These measurements are the first to suggest that wave groups and associated infragravity wave forcing may significantly influence the dynamics of small coastal plumes in the surfzone, affecting salinity distributions and cross-shore plume extent, and adding a time scale not previously considered in wave-plume studies (Flores et al., 2022).

Although progress has been made based on modeling (e.g. Rodriguez et al., 2018; Moghimi et al., 2019) and a few field studies (e.g. Wong et al., 2013; Kastner et al., 2019; Flores et al., 2022), our understanding of river-wave interactions in the surfzone remains incomplete. Specifically, we have yet to achieve a comprehensive description of the timescales relevant to these interactions and the fate of freshwater in the nearshore. River-wave interactions are influenced by several factors, including the variability in river discharge, offshore wave climate, tides, winds, and surfzone dynamics, encompassing processes with timescales ranging from a few seconds (i.e., individual waves) to several days (wave climate). In this work we use *in situ* and remote (drone-based) observations at the mouth of the Maipo River to investigate river-wave in the surfzone interactions with a focus on timescales associated to wave groups (infragravity), tides (ebb and flood) and the offshore wave forcing. We highlight the role of the tidal phase on plume development and the influence of the infragravity wave forcing on salinity modulations within the surfzone.

1.3 Thesis Structure, Goals and Hypothesis

The document is organised in chapters as follows.

- **Chapter 1:** Motivation about the importance of coastal environments, and the study of river plumes hydrodynamics. Thesis structure, goals and hypothesis.
- **Chapter 2:** State of the Art. Brief summary of coastal dynamics and research on small-scale river plumes.
- **Chapter 3:** Methods. Field campaign and data collection. Data processing and analysis.
- **Chapter 4:** Results.
- **Chapter 5:** Discussion.
- **Chapter 6:** Conclusions.

The general goal of this study is to **assess the influence of nearshore wave forcing on the discharge of the Maipo river in the surfzone, at synoptic, tidal and infragfravity time-scales**. The specific goals are listed below.

1. Relate wave climate at a synoptic time-scale with the dispersion of the river plume via in-situ measurements.
2. Analyse the impact of tides, gravity waves and infragravity waves on the pressure and salinity signals at the mouth, including the estuary and surf zone.

The hypotheses of this work are the following.

1. Infragravity waves influences the hydrodynamics of the plume of the Maipo river in the surfzone.
2. Infragravity-driven dynamics of the plume are modulated by the tide.
3. Infragravity-driven dynamics of the plume are modulated by the offshore wave climate.

Chapter 2

State of the Art

2.1 Ocean Waves

2.1.1 Definitions

Waves in the sea can be succinctly defined as the variation of the free surface that occurs for different length and time scales. According to the linear theory of waves proposed by Airy, the oscillations of the sea can be described from a sinusoidal function, as shown in the figure 2.1.

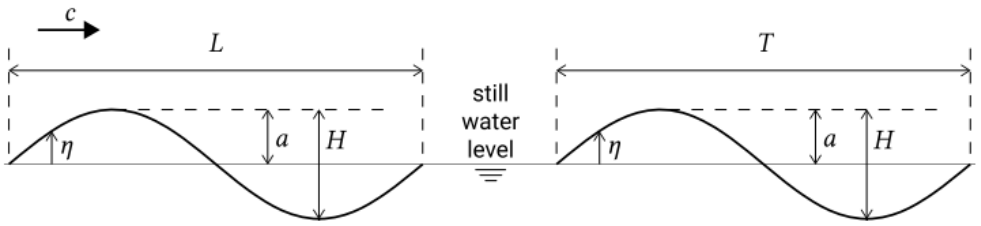

Figure 2.1: Sea Oscillation Definitions
Source: Coastal Dynamics, Judith Bosboom & Marcel J.F. Stive

Where η defines the oscillation of the free surface, being a the amplitude of this wave and defining the height of wave H as twice said amplitude. In addition, T, L and c correspond to the period, the length and the speed of wave propagation, respectively. Additionally, the angular frequency $\omega = 2\pi/T$ and the wave number $k = 2\pi/L$ are defined. This defines the oscillation of the free surface as indicated in the equation 2.1.

$$\eta = a \sin(\omega t - kx) \tag{2.1}$$

2.1.2 Wave Dispersion

Under the assumption of irrotational and incompressible flow, the dispersion relation is deduced (equation 2.2), which relates the period and the wavelength —indirectly through ω and k, respectively— with the influence of the depth h.

$$\omega^2 = gk \tanh(kh) \tag{2.2}$$

Since wave frequency ω stays constant as waves propagate towards shallower waters, the decrease in wavelength L implies a decrease in wave velocity c.

2.1.3 Wave Spectrum

The spectrum of spatio-temporal scales of these oscillations allude to different generation mechanisms of these waves. The figure 2.2 shows the spectrum of sea oscillations, highlighting the energy contribution associated to each period, also identifying the name of each band and its generation and restoration mechanisms. For this study, the relevant oscillations are gravity waves, infragravity and tides.

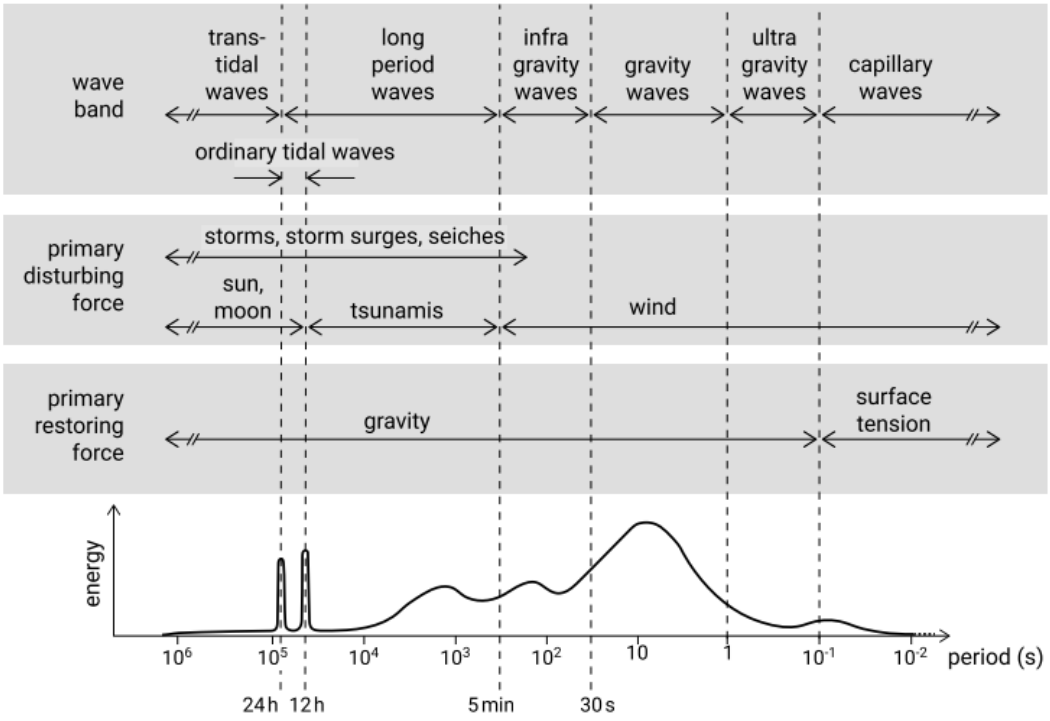

Figure 2.2: Ocean Waves Spectrum
Source: Coastal Dynamics, Judith Bosboom & Marcel J.F. Stive

Gravity Waves

They correspond to the waves that are visually identified on the beaches and in the sea with periods between $1[s]$ and $30[s]$. These oscillations are generated by winds and gravity is the restoring force. Locally generated gravity waves are relatively short, random and irregular; so called "sea" waves. When sea waves are generated offshore, they travel to the coast and undergo wave transformation (see Section 2.2), turning into faster, longer and more regular "swell" waves due to frequency dispersion and damping. As Figure 2.2 shows these waves are the most contributing in terms of energy.

Infragravity Waves

These oscillations are longer waves than gravity, with periods ranging from $30[s]$ to $5[min]$. They are generated due to gravity wave interactions. Despite being not energetically relevant in deep waters, these waves are important for coastal processes as they grow in the surfzone. Further explanation in Section 2.4.

Tides

Tides are generated by the mutual gravitational attraction of the earth and the moon, and of the earth and the sun. There are hundreds of tidal constituents (i.e., different frequencies components), nevertheless the main one for most locations is the principal lunar semidiurnal constituent $M2$ with a period of $12.42[h]$.

2.1.4 Short-term Wave Statistics

Since ocean waves are neither monochromatic or regular in amplitude, (i.e., random waves), it is necessary to summarise sea oscillation signals statistically. If we describe the short-term variations in a statistical way by taking average parameters, in order for the averages to be representative of the sea state, the record should be short enough to be statistically stationary. On the other hand the record should be long enough to get reliable averages. A record duration of $20[min]$ is commonly used for measure ocean (gravity) waves.

There are two approaches to characterise a wave record in terms of its short-term statistics:

1. **Wave-by-wave:** Direct analysis of the time series and considering it as a sequence of individual waves.
2. **Spectral:** Based on the fact that the surface oscillations can be described as a summation of infinite number of sine waves with different heights, periods and directions.

Wave-by-Wave Analysis

Based on the statement that for a stationary signal the mean should be constant, once the water elevation signal is demeaned, individual waves can be defined as having a wave height equal to the difference in elevation between the crest and the trough. The wavelength and wave period are the distance and time (respectively) between two subsequent downward or upward zero-crossings. Average parameters are derived from this process, of which the most obvious probably is the mean wave height. Nevertheless, the mean wave height is

not used that often. Of more practical use is the significant wave height H_s described in Equation 2.3, where H_i is the i-th wave, order from the largest ($i = 1$) to the smallest, and N is the total number of waves.

$$H_s = \frac{1}{N/3} \sum_{i=1}^{N/3} H_i \tag{2.3}$$

Spectral Analysis

The oscillatory surface elevation η can described as a Fourier series, as in Equation 2.4.

$$\eta = \sum_{n=1}^{N} = a_n \cos(2\pi f_n t + \phi_n) \tag{2.4}$$

Where $f_n = n/T_r$ is the frequency defined as the ratio between the n-th mode and the record duration T_r. This relation also defines the discretization of the frequency domain so $\Delta f_n = 1/T_r$, which equals the smallest frequency $f_{min} = 1/T_r$. Furthermore, as the signal is not continuous, i.e., the measurements are set to a certain sample frequency f_s, there is a restriction for the highest frequency to be determined with the record, called the Nyquist frequency that equals half the sample frecuency, so $f_{max} = f_s/2$.

Considering the amplitudes of various frequency components, the spectrum of wave energy can be computed as the variance of the oscillatory surface elevation in the Fourier series form. This is a variance density per unit of frequency interval, so the spectrum is constant for $\Delta f \to 0$, as Equation 2.5 shows.

$$\lim_{\Delta f \to 0} \frac{a_n^2}{2\Delta f} = E(f_n) \tag{2.5}$$

By integrating the spectrum in the frequency domain, the total variance σ^2 is recovered (Equation 2.6). Therefore, the density spectrum of a certain frequency is the contribution of that frequency variance to the total variance of the signal.

$$\int_0^\infty E(f)df = \sigma^2 \tag{2.6}$$

The variance σ^2 corresponds to the zero-th spectral moment, so that in a more general way the moments are described as follows.

$$m_n = \int_0^\infty f^n E(f)df \tag{2.7}$$

From spectral moments several wave parameters can be determined. The most commonly used is the spectral wave height showed in Equation 2.8.

$$H_{m0} = 4\sqrt{m_0} \tag{2.8}$$

To compute the spectrum of a water elevation signal the Fourier Transform can be used. This transforms a signal $\eta(t)$ in the time domain to its representation in the frequency domain $g(\xi)$, as Equation 2.9 shows.

$$g(\xi) = \frac{1}{\sqrt{2\pi}} \int_{-\infty}^{+\infty} \eta(t) e^{-i\xi t} dt \tag{2.9}$$

In practice the Fast Fourier Transform (FFT) algorithm is used to compute the transform of the signal.

2.1.5 Wave Groups

Wave groupiness is caused by the interference between waves of different wavelength. The broader the spectrum the less clearly the groups can be identified, since the waves are more irregular. Thus, wave grouping is prominent in swell. The period of the groups can be computed from the differences frequencies as in Equation 2.10, where ω_1 and ω_2 are the frequencies of the shorter and longer wave, respectively.

$$\omega_{group} = \omega_2 - \omega_1 \Rightarrow T_{group} = \frac{2\pi}{\omega_2 - \omega_1} \tag{2.10}$$

For swell waves, due to the slight differences in wave frequencies the group periods T_{group} correspond to the infragravity band of the wave spectrum (see Section 2.1.3). Indeed, wave groupiness is a primordial phenomena for the generation of infragravity waves (see Section 2.4).

One important dynamical characteristic of wave groups is that energy is carried in the group and not in each individual wave, i.e., energy fluxes at groups velocity c_g and not at phase velocity c. The ratio between both velocities according to Airy wave theory is defined as n and is shown in Equation 2.11.

$$n = \frac{c_g}{c} = \frac{1}{2}\left(1 + \frac{2kh}{\sinh(2kh)}\right) \tag{2.11}$$

This equation shows the dependence of the velocity ratio with water depth. For deep waters group velocity is half of phase velocity. For shallow waters, $n = 1$ and velocities are equal.

2.2 Wave Transformation

As offshore generated waves travel to the coast they undergo several processes. These mainly relate to the interaction of the waves with the propagation medium topology, (i.e., bathymetry) and derived phenomena, changing wave height, length and direction. As waves propagates to the coast the energy is conserved, except for the dissipation due to bottom friction and wave breaking. The energy balance assuming a stationary process is shown in Equation 2.12.

$$\frac{\partial}{\partial x}(Ec_g \cos(\theta)) + \frac{\partial}{\partial y}(Ec_g \sin(\theta)) = -D_f - D_w \tag{2.12}$$

Where $E = \rho g H^2/8$ is the wave energy, θ is the wave angle, and D is the dissipation due to bottom friction and wave breaking (subscripts f and w, respectively).

2.2.1 Refraction

Given that waves travel with a certain angle θ i.e., wave fronts are not parallel to the coast, water depth is not constant in a wave front. Thus, considering the dispersion relation (Equation 2.2), the part of the wave front that is in deeper (shallower) water travels faster (slower). This difference in the speed of the wave induces a twist of the wave front, making it increasingly parallel to the coast. Eventually, all wave arrive the coast with a wave angle $\theta = 0$.

This phenomena is called *refraction* and within wave theory its simple definition is the change in direction as of a wave passing from one medium to another caused by its change in speed. In this case, the change of medium corresponds to a change in water depth.

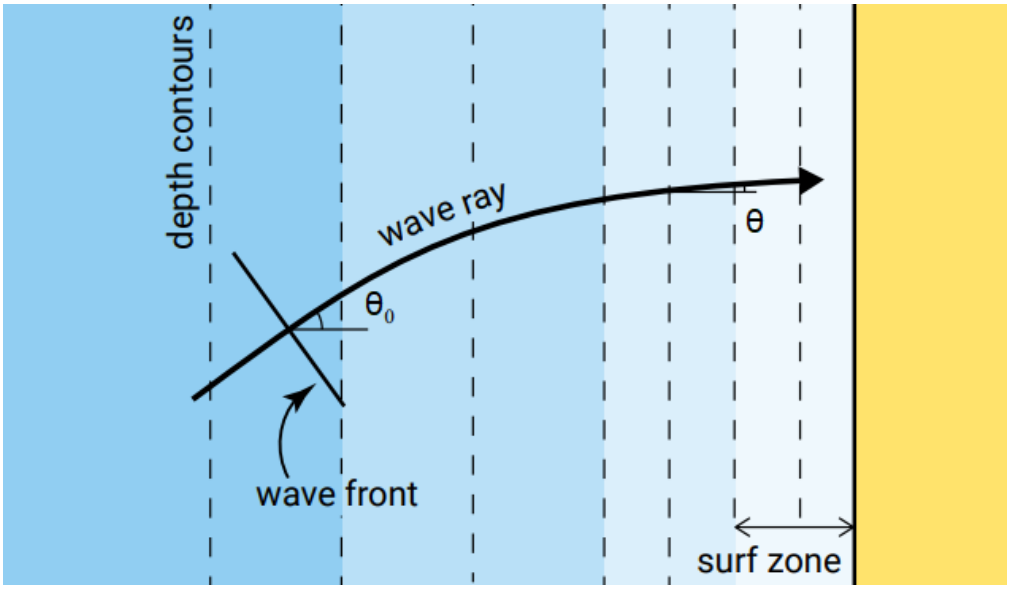

Figure 2.3: Refraction Diagram
Source: Adapted from Coastal Dynamics, Judith Bosboom Marcel J.F. Stive

The change in wave direction follows the Snell's law (Equation 2.13).

$$\frac{\sin(\theta_2)}{c_2} = \frac{\sin(\theta_1)}{c_1} \tag{2.13}$$

2.2.2 Shoaling

When a wave is approaching to the coast its speed will be affected by the bottom when the water depth becomes less than about half the wavelength (deep-shallow water criteria). A decrease in water depth implies a decrease in velocity and wave length due to the dispersion relation (Equation 2.2). Following the energy balance (Equation 2.12) a decrease in velocity produces an increase in wave energy, thus in wave height. This reduction in wave length (and speed) and increase in height is called *shoaling*.

2.2.3 Breaking

As waves approach to the coast they increase in height due to shoaling. This also contributes to increase the steepness of the waves, producing an instability and finally inducing wave breaking. The increase in wave height implies an increase in wave orbital velocities. Furthermore, shoaling induces a decrease in phase velocity, thus eventually particles will travel faster than the wave front.

Breaking waves propagate through the surfzone as a *roller*, which is a layer of air-water mixture — highly chaotic — that travels at phase velocity towards the shore in the top of the water column. The roller dissipates energy as heat and sound. This dissipation process in the surfzone is the main way in which waves lose energy. Battjes (1975) showed that the breaking process depends on the *surf similarity parameter* ξ (Equation 2.14) proposing that the way waves break differs depending on ξ as Figure 2.4 shows.

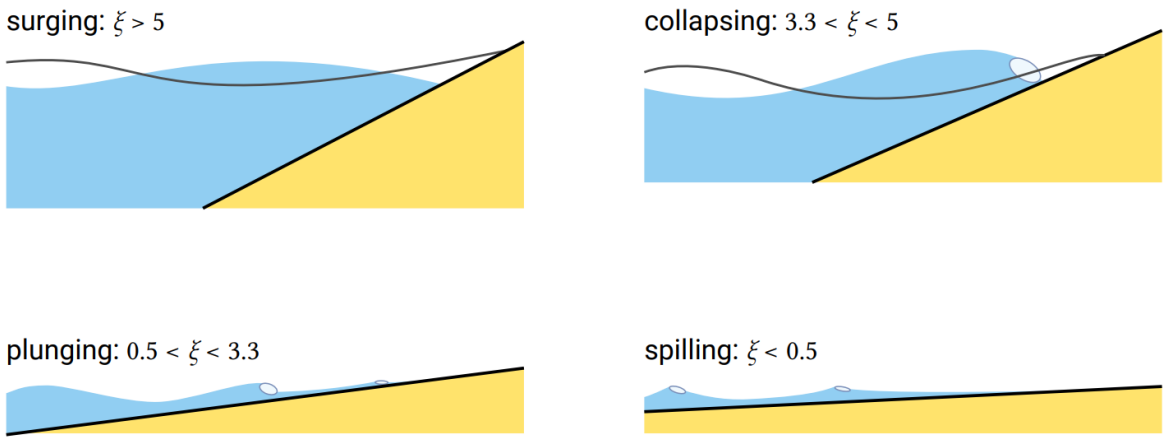

Figure 2.4: Breaker types depending on surf similarity parameter
Source: Adapted from Coastal Dynamics, Judith Bosboom Marcel J.F. Stive

$$\xi = \frac{m}{\sqrt{H_s/L}} \tag{2.14}$$

Miche (1944) developed a criteria to determine the limiting wave steepness based on the nonlinear wave theory, where the results simplified for shallow water proposed a breaker index γ equal to the ratio between wave height and water depth (Equation 2.15).

$$\gamma = \frac{H_b}{h_b} \tag{2.15}$$

In the work proposed by Miche (1944) $\gamma = 0.88$, whereas using solitary wave theory the value slightly differs to $\gamma = 0.78$. Battjes (1975) proposed that the breaker index depends on the surf similarity parameter as Equation 2.16 shows.

$$\gamma = 1.06 + 0.14 \ln \xi \tag{2.16}$$

Other authors (e.g., Battjes and Stive, 1985; Nairn, 1990) (Equations 2.17 and 2.18, respectively) proposed formulations for the breaker index based on the deepwater stepness:

$$s_0 = H_{rms0}/L_0$$

$$\gamma = 0.5 + 0.4 \tanh(33 s_0) \tag{2.17}$$

$$\gamma = 0.39 + 0.56 \tanh(33 s_0) \tag{2.18}$$

2.3 Setup and Currents

2.3.1 Radiation Stress

Radiation stress is defined as *the excess of momentum flux due to the presence of waves* (Longuet-Higgins and Stewart, 1962). This quantity is a depth-integrated and wave-averaged second order symmetric tensor. The components of the radiation stress tensor are shown in Equations 2.19, 2.20 and 2.21.

$$S_{xx} = E\left[n(\cos^2\theta + 1) - \frac{1}{2}\right] \tag{2.19}$$

$$S_{yy} = E\left[n(\sin^2\theta + 1) - \frac{1}{2}\right] \tag{2.20}$$

$$S_{yx} = S_{xy} = E\left[n\cos\theta\sin\theta\right] \tag{2.21}$$

where $E = \rho g H^2/8$ is the wave energy, θ is the wave direction, and n is the ratio between the group and phase velocities given by Equation 2.11. Since radiation stress is proportional to the square of the wave height, it will increase in the shoaling zone, and will decrease in the surfzone.

2.3.2 Wave Setdown and Setup

Considering an idealised beach uniform in the y-direction, the cross-shore momentum equation neglecting bottom stress and currents ends up being a balance between pressure and radiation stress (Equation 2.22).

$$0 = -h\frac{\partial p}{\partial x} - \frac{\partial S_{xx}}{\partial x} \tag{2.22}$$

where $p = \rho g(h + \bar{\eta})$ is the hydrostatic pressure, i.e., the pressure given by the mean water level $\bar{\eta}$—since radiation stress considers the pressure component due to waves—. After algebraic manipulation pressure term in Equation 2.22 is written in terms of $\bar{\eta}$, as Equation 2.23 shows.

$$0 = -\rho g h\frac{\partial \bar{\eta}}{\partial x} - \frac{\partial S_{xx}}{\partial x} \tag{2.23}$$

Therefore, given that radiation stress changes in the cross-shore direction due to shoaling and breaking, a change in the mean water level $\bar{\eta}$ must exist so the momentum balance is valid.

As waves undergo shoaling the increase in height and S_{xx} increases, thus $\bar{\eta}$ decreases. Once waves break, they decrease in height due to dissipation, therefore within the surfzone and approaching towards the coast $\bar{\eta}$ increases. These phenomena are called *setdown* and *setup*, respectively.

The pressure gradient produced by the wave setup induces an offshore directed current that takes places in the lower part of the water column, which is called undertow. This current balances onshore mass flux caused by broken waves, creating a circulation pattern within the surfzone, as Figure 2.5 depicts.

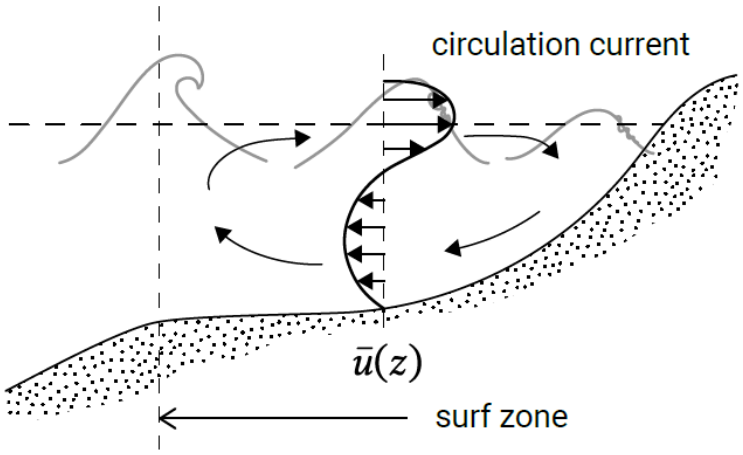

Figure 2.5: Undertow and broken waves driven mass flux
Source: Coastal Dynamics, Judith Bosboom Marcel J.F. Stive

2.3.3 Alongshore Currents

Similarly as in the cross-shore direction, a momentum balance in the alongshore direction is showed in Equation 2.24.

$$\frac{\partial S_{yx}}{\partial x} + \bar{\tau}_{b,y} = 0 \tag{2.24}$$

Where $\bar{\tau}_{b,y}$ is the bed shear stress in the y direction, that is generated due to a current. This current is induced, indeed, by the cross-shore variation of the shear component of the radiation stress S_{yx} and is balanced by the resulting bed shear stress. Thus, in order to a generate an alongshore current S_{yx} has to vary in the x coordinate.

Since S_{yx} is constant for a conservative wave energy flux scenario in an uniform beach (i.e., no changes in bathymetry across the alongshore coordinate) , alongshore wave-driven currents are negligible in deep waters and in the shoaling zone, whereas they are important within the surfzone. This statement is proven as follows.

Considering the energy flux balance (see Equation 2.12) with no dissipation (i.e., $D_w = D_f = 0$) and introducing the group and phase speed ratio n (see Equation 2.11) we obtain:

$$\frac{\partial}{\partial x}(Enc\cos(\theta)) + \frac{\partial}{\partial y}(Enc\sin(\theta)) = 0$$

For an uniform beach the second term on the left hand is zero. Furthermore, considering Snell's law (Equation 2.13) with the deep-water celerity c_0 and wave direction θ_0:

$$\frac{\partial}{\partial x}(En\cos(\theta)\frac{c_0\sin(\theta)}{\sin(\theta_0)}) = 0$$

Since c_0 and θ_0 are constants they can me moved outside the derivative. Then, considering the definition of the shear component of the radiation stress S_{yx} (Equation 2.21) we finally obtain:

$$\frac{\partial S_{yx}}{\partial x} = 0$$

As mentioned before, this demonstration makes the assumption of non-dissipative waves. As waves break, an important amount of energy is dissipated, which results in a change in the shear component of radiation stress in the cross-shore direction and corresponding alongshore currents.

2.4 Infragravity Waves

According to Bertin et al. (2018) there are three generation mechanisms of infragravity waves in the surfzone, where all mechanisms are related to wave groups somehow. Nevertheless, two of them — *Bound Wave Release* and *Moving Breakpoint*— regard the wave groupiness influence in wave breaking, whereas the third one — *Bore Merging* — relates to the difference in wave celerity given the difference in breaking wave heights, taking place within the surfzone and not at the breakpoint as the other two.

2.4.1 Bound Wave Release

The presence of groups in incident gravity waves may force a *bound* wave which frequency matches the group frequency (e.g., Biesel, 1952; Longuet-Higgins and Stewart, 1962). Although being small in amplitude, this secondary wave increases in height within the surfzone. Due to wave breaking the bound wave is no longer travelling phase-locked, i.e., it is released and propagate as a free wave (e.g., Janssen et al., 2003; Battjes et al., 2004). The bound wave is in anti-phase with the wave group envelope as shown in Figure 2.6.

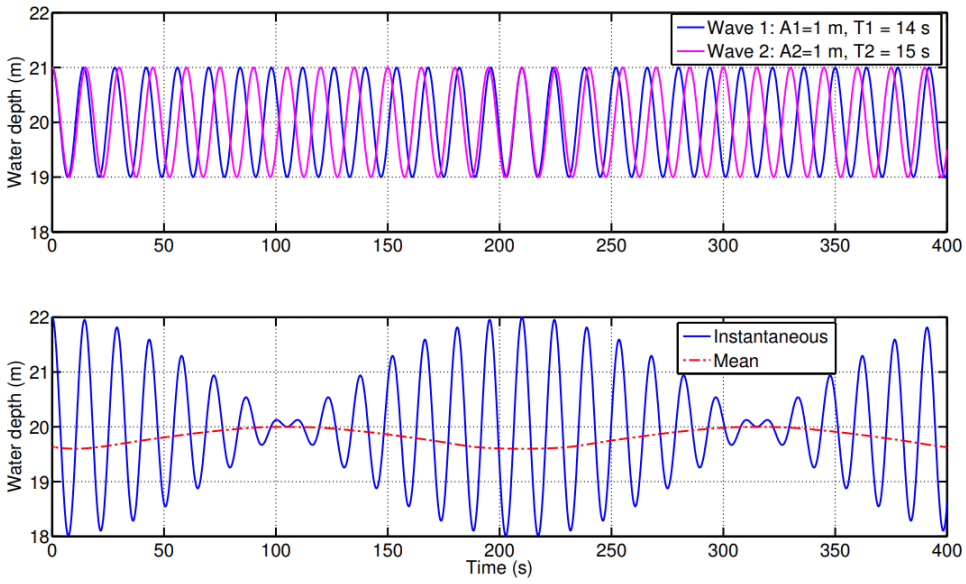

Figure 2.6: Bound Wave in a Group. Representation of the superposition of bi-chromatic waves and its mean representing a Bound Wave that its in anti-phase with the group envelope. Source: Bertin et al. (2018)

Battjes et al. (2004) proposed that this mechanism is dominant for mild slope regimes, i.e., when the normalised bed slope parameter β_b (Equation 2.25, with m being the beach slope) is below 0.3.

$$\beta_b = \frac{m}{\omega}\sqrt{\frac{g}{h}} \tag{2.25}$$

2.4.2 Moving Breakpoint

The groupiness of waves causes a time-variation in the position of the breakpoint, since higher waves would break further offshore than lower ones. This shift of the breakpoint position implies a time-variation of the radiation stress gradient (i.e., the momentum imposed by the waves) that must be balanced with a time-variation in wave setup (Bertin et al., 2018). This mechanism is dominant for steep slope beaches, with $\beta_b \geq 1$ (Battjes et al., 2004). For this generation mechanism, the IG wave is in phase with the group envelope, as Figure 2.7 depicts.

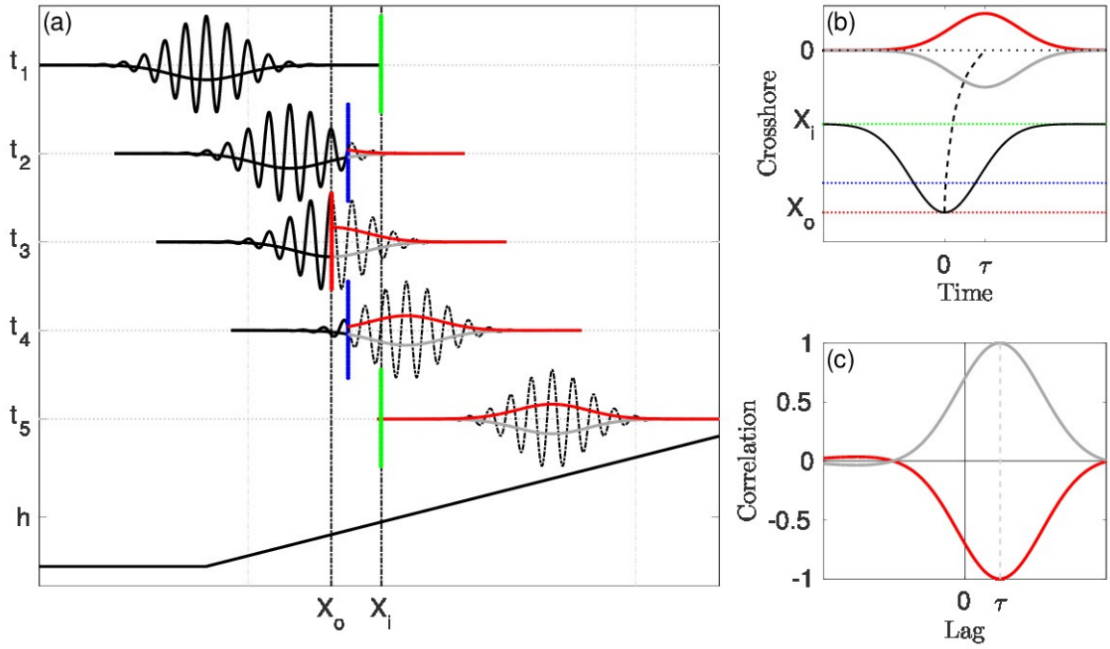

Figure 2.7: Scheme of Bound Wave Release and Moving Breakpoint. (a) Wave group (in black) travelling to the shore and breaking at points x_o and x_i. Red line shows setup increase due to Moving Breakpoint mechanism. Grey line shows Bound Wave Release mechanism. (b) Time-variation of cross-shore position of the breakpoint (in black). In red and grey the effect in shoreline excursion of Moving Breakpoint and Bound Wave Release, respectively. (c) Correlation between breakpoint position and IG generation mechanisms effect on shoreline excursion. Source: Moura and Baldock (2017)

2.4.3 Bore Merging

After breaking, short waves reorganise themselves in the inner surfzone into bores (breaking wave front, resembling to a hydraulic jump). In random wave fields, due to amplitude dispersion, larger bores travel faster than smaller ones. Therefore, when there is enough space (or time) larger bores will eventually catch up with smaller ones (Brocchini and Baldock, 2008); i.e., the large bore overtakes the small bore ahead and merge together into a single wave front (Bertin et al., 2018).

This nonlinear process leads to an increase in the wave period in the surf zone, and as such contributes to an energy transfer from short wave frequencies to IG wave frequencies (Bertin et al., 2018).

2.5 Small-Scale Plume Hydrodynamics

Plume hydrodynamics theory has been focused mainly on large-scale systems, where due to large outflow rates and geometric dimensions, nearshore wave forcing is seldom relevant in the final destination of the freshwater. Other phenomena such as Coriolis effect, winds, and tides are generally more important for large-scale plume hydrodynamics.

Small-scale rivers often discharge into energetic surfzone regions where nearshore wave forcing and wave driven processes strongly influence plume hydrodynamics (Wong et al., 2013; Delpey et al., 2014; Rodriguez et al., 2018; Kastner et al., 2019; Flores et al., 2022; Kastner et al., 2022). Small-scale river mouths are comparable to wave forcing in terms of size (vertical and horizontal representative scales) and force (river outflow momentum and radiations stress gradients). Therefore, nearshore wave forcing is determinant in the final destination of small-scale river freshwater input in the coastal environment.

As waves approach to the coast they brake, energy is dissipated and radiation stress decreases towards the shore. This change in radiation stress cross-shore and shear components induce an onshore directed resultant force and alongshore currents, respectively (see Section 2.3). The latter two enhance the retention of the plume within the surfzone (Wong et al., 2013; Rodriguez et al., 2018; Flores et al., 2022).

The idealised numerical simulations by Rodriguez et al. (2018) compared the structure of a freely expanding plume (i.e., no waves) and a plume influenced by symmetric wave forcing (i.e., wave fronts parallel to the coastline, thus no wave driven alongshore currents). Results showed that as expected nearshore wave forcing induces a retention of the plume in the cross-shore direction with a corresponding expansion in the alongshore direction, as Figure 2.8 depicts.

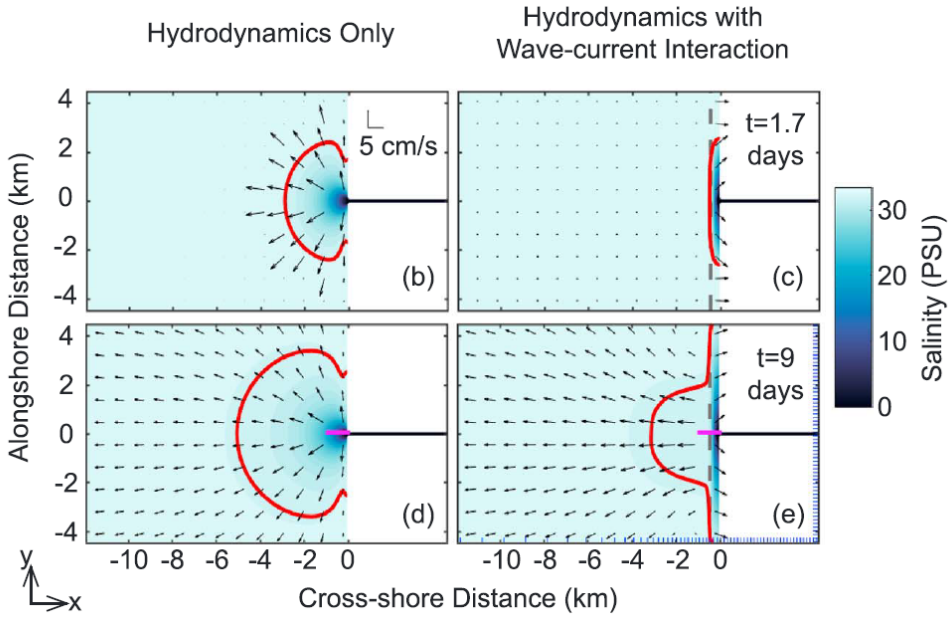

Figure 2.8: (b–e) Surface salinity $[psu]$ and surface current vectors $[cm/s]$ after 1.7 (b, c) and 9 (d, e) days of $Q = 20[m^3/s]$. The plume edge (red) is taken to be the 97^{th} percentile of the salinity range. (b) and (d) show results for the hydrodynamics-only solution, while (c) and (e) show coupled model results which simulate wave-current interactions with $H_s = 1[m]$. Source: Adapted from Rodriguez et al. (2018)

Rodriguez et al. (2018) showed that the percentage of freshwater that is retained in the surfzone is related to the ratio of river momentum flux and wave momentum flux (radiation stress). Large part of the freshwater input escapes the surfzone when river momentum exceeds the incident wave momentum, whereas most freshwater is entrained into the surfzone when the opposite occurs, as Figure 2.9 shows.

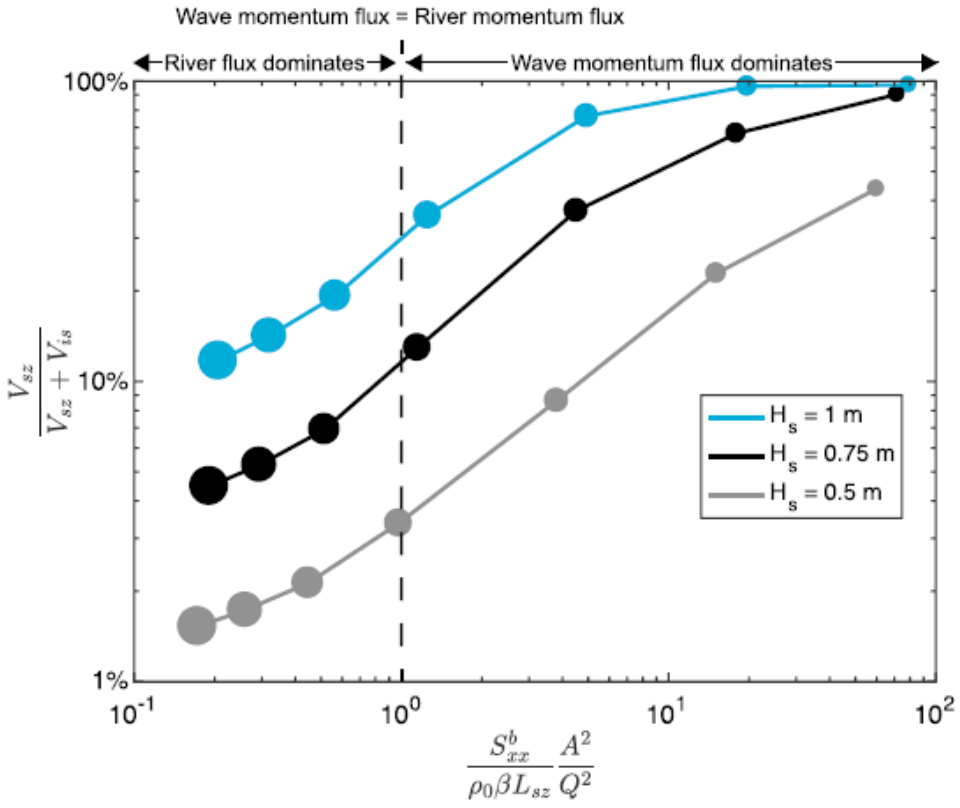

Figure 2.9: Percentage of freshwater volume within the surf zone as a function of the ratio of the wave and river momentum fluxes for simulations varying both Q and H_s. Results are plotted on log scales to display the range of values. Circle size indicates flow rate, which ranges from $100[m^3/s]$ (largest) to $5[m^3/s]$ (smallest circles). Source: Rodriguez et al. (2018).

Besides numerical simulations, field studies —although very scarce— have also reported surfzone trapped river plumes (e.g., Wong et al., 2013; Kastner et al., 2019; Flores et al., 2022). Conceptual models have been proposed based on field measurements to predict if river water is transported outside of the surfzone (e.g., Wong et al., 2013; Kastner et al., 2019). These models use length scales based on the river outflow momentum and the wave-driven momentum, which are compared to the surfzone width (L_{SZ}) to assess the potential for river water to escape the surfzone (Wong et al., 2013; Kastner et al., 2019).

Wong et al. (2013) proposed a cross-flow length scale (L_a), determined by the discharge momentum and the wave-driven alongshore velocity (Jones et al., 2007; Wong et al., 2013), defined as Equation 2.26 shows,

$$L_a = \frac{M_j^{1/2}}{U_{SZ}} \tag{2.26}$$

where $M_j = Q_j U_j$ is the momentum of the discharge jet and U_{SZ} is a representative velocity of the alongshore currents. Using measurements at the mouth of a small creek in California and numerical simulation results, Wong et al. (2013) proposed that if $L_{SZ}/L_a > 10$ river water is completely retained within the surfzone. Figure 2.10 shows the latter.

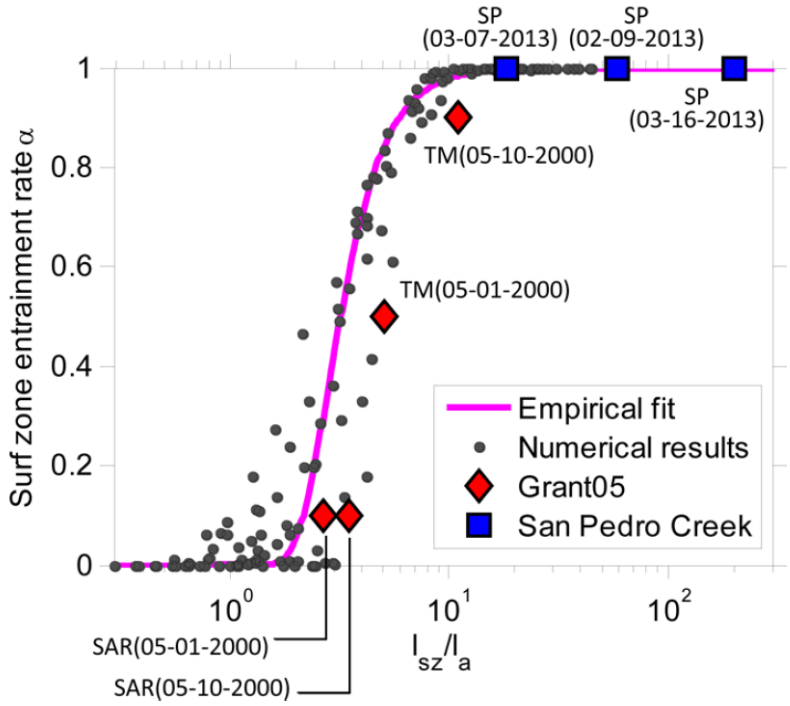

Figure 2.10: Scatter plot of surf zone entrainment rate α against the quotient of surf zone width and jet cross-flow length scale L_{SZ}/L_a. The filled circles are results from numerical experiments. The solid line is the empirically fitted line. The markers are dye study results. Source: Wong et al. (2013)

Hetland (2010) proposed a near-field plume length (L_{NF}) based on discharge momentum and plume buoyancy, defined as in Equation 2.27

$$L_{NF} = \frac{u_0^{3/2} Q^{1/4}}{g'^{1/2} w_e^{3/4}} \tag{2.27}$$

where u_0 and Q are the river discharge velocity and flowrate, respectively. The reduced gravity $g' = g\Delta\rho/\rho_0$ takes into account the density difference between the river water and the ambient seawater. The entrainment rate w_e quantifies the importance of momentum and buoyancy loss of the jet due to mixing in the shear layer.

This lenght scale was used by Kastner et al. (2019) to describe plume escapes at the Quinault River, Oregon. They found that if $L_{NF}/L_{SZ} > 1$ the river water escapes the surfzone as discharge momentum overcomes the wave forcing. Another way to understand this ratio between the near-field lenght and the surfzone width is that in order for the plume to escape it has to reach the breakpoint as with $Fr > 1$. Figure 2.11 shows the comparison of this two scales.

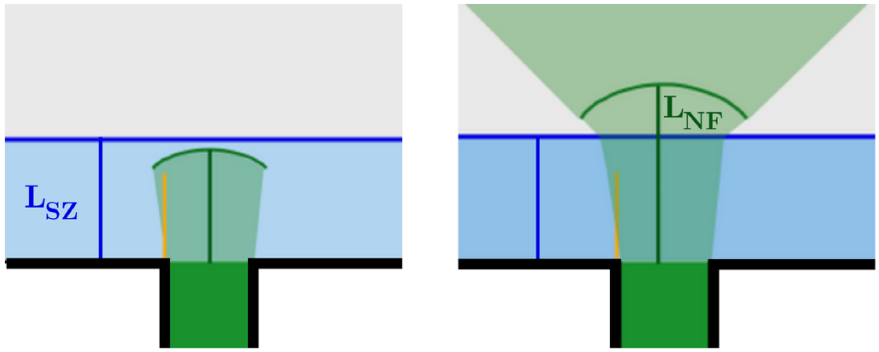

Figure 2.11: Surf zone width indicated by the blue line and the near-field length by the green line. Panel (a) shows wave dominance and (b) shows river dominance. Source: Adapted from Kastner et al. (2019)

Chapter 3

Methods

3.1 Study Area and Field Campaign

An observational field campaign was conducted during September 5-11, 2021, at the mouth of the Maipo River in Central Chile (Figure 3.1).

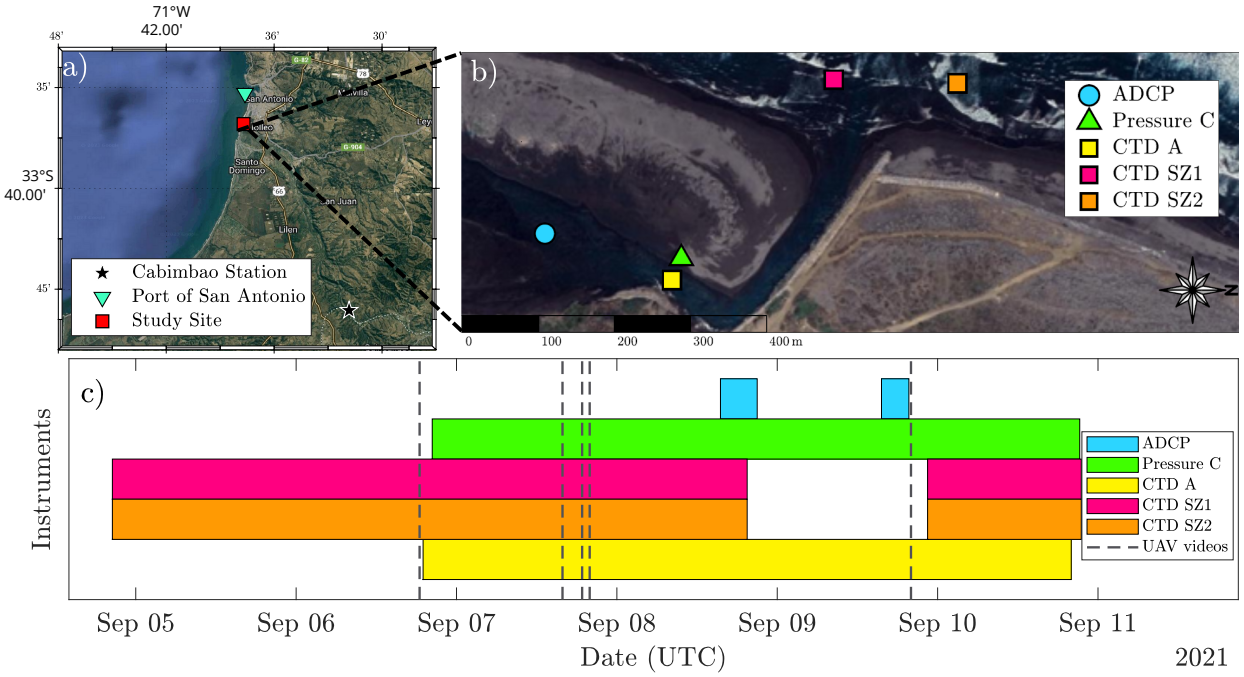

Figure 3.1: Study area and observational field campaign. (a) Study area. (b) Study site, instrument deployment locations. (c) Instrument measurement times (coloured bars) and rectified drone flights (dashed lines).

The Maipo River originates in the Andes, and drains a 15000 $[km^2]$ watershed that contains Santiago (Chile's capital with 35% of the country's population), important agricultural areas, and high industrial activity (Peña-Guerrero et al., 2020). There is growing concern regarding the water quality of the Maipo River because of

persistent and extensive interventions throughout its trajectory from the mountains to the sea (e.g., Rosegrant et al., 2000; Cai et al., 2006). The Maipo river mouth is located $1[km]$ south of the Port of San Antonio (Chile's largest port), and the planned construction of a port extension next to the inlet and protected wetlands makes this site of great national interest.

The Maipo is a small low-inflow river with annual average flow rate at the gauging station closest to the mouth (Cabimbao, BNA 0578001-7, 20 km upstream) of $\sim 50[m^3/s]$ over the past decade. In recent years, the annual average flow rate has decreased to $\sim 30[m^3/s]$ as a consequence of water extractions and the mega-drought central Chile has experienced since 2010 (e.g., Garreaud et al., 2017, 2020). The flow regime near the river mouth is characterised by a highly seasonal discharge due to episodic rainfall events in winter and snow-melt in summer (Peña-Guerrero et al., 2020). The Maipo River discharges into an energetic and exposed coast, with mean values of offshore wave height and peak period of $1.5[m]$ and $12[s]$, respectively (Beyá et al., 2016). The wave forcing generally propagates northeastward generating northward alongshore currents (e.g. Flores et al., 2022). Similar to many other regions with mediterranean climates, the strong wave activity combined to the low and sharply seasonal discharge result in the formation of a large sand bar at the mouth and a bar-built estuary (Figure 3.1a,b).

The field observations consisted of *in situ* and remote sensing measurements. *in situ* data were collected in the surfzone and in the inlet (Figure 3.1a). The surfzone measurements consisted of surface CTDs (conductivity, temperature, and depth) located (i) directly offshore of the river mouth and in the trajectory of the outflow jet $(SZ1)$, and (ii) approximately $200[m]$ north of the river mouth $(SZ2)$ (Figure 3.1a). The instrumental setup deployed in the inlet consisted of a mooring with surface and bottom CTDs and a pressure sensor approximately $100[m]$ upstream of the entrance of the outflow channel (see yellow square and green triangle in Figure 3.1a). A down-looking ADCP (Acoustic Doppler Current Profiler) was also deployed in the inlet $\sim 200[m]$ upstream of the top-bottom CTD array at location L (Figure 3.1a). The ADCP measured at $1[Hz]$ with vertical resolution of $10[cm]$. The velocity data was then depth-averaged for subsequent calculations. Surfzone and inlet salinity was then derived from the CTD measurements. The sampling interval at locations $SZ1$ and $SZ2$ were set to $15[s]$ during September 5-8. These instruments were then recovered and redeployed on September 10, with a sampling interval of $4[s]$. The sampling rates for the instruments deployed in the inlet were $0.05[Hz]$, $16[Hz]$ and $1[Hz]$ at locations A, C and L, respectively. The remote sensing data consisted of a series of drone images and videos collected while *in situ* instruments were in the water. Drone imagery was obtained using a recreational DJI Mavic Air 2 quadcopter. The drone flights aimed to capture the discharge channel, near-field plume and surfzone, and were conducted primarily during ebb tides to capture the plume as it entered the surfzone (see Section 3.2.1). The measurement periods of the instruments are shown in Figure 3.1).

Wave climate data and tidal elevation are recovered at the port of San Antonio, located $1[km]$ north of the river mouth. Flores et al. (2022) found that wave climate measured by an ADCP deployed in 13 m of water off the river mouth agreed well with the data obtained from the San Antonio Port. River discharge at the closest gauging station was obtained from the Dirección General de Aguas de Chile (Cabimbao, BNA 05748001-7, $\sim 20[km]$ upstream).

3.2 Data Analysis

3.2.1 Drone imagery

Drone images and videos were rectified using the CIRN Quantitative Coastal Imaging Toolbox (Bruder and Brodie, 2020) and 5 to 7 geo-referenced ground control points along the sandbar and beach. A total of 18 flights were made, however, not all of them were rectifiable as ground control points could not always be included in the images to properly document plume movement. Unrectified videos were used to qualitatively identify plume motion, wave breaking, and wave propagation.

As turbidity in the Maipo is typically very high, the river plume can be easily identified based on colour differences between the sediment laden plume waters and the ocean water in the majority of the drone videos (e.g., Figure 3.1b). To aid plume detection in rectified and non-rectified footage, we used the Normalised Difference Turbidity Index (NDTI), which highlights turbidity by combining red and green RGB bands as Equation shows (e.g., Lacaux et al., 2007). Cross-shore and alonghshore timestacks were constructed from the rectified video imagery, which were used to identify plume presence and wave forcing in the surfzone (e.g., Flores et al., 2016; Moura and Baldock, 2017; Flores et al., 2022).

$$\text{NDTI} = \frac{\text{Red} - \text{Green}}{\text{Red} + \text{Green}} \tag{3.1}$$

3.2.2 Signal analysis

Time-frequency analyses were performed by computing power spectral densities (PSD) and continuous wavelet transforms (CWT) of the relevant time series (e.g., salinity, pressure, and drone timestack). The PSDs were computed using a Fast Fourier Transform (FFT) and were used to analyse short duration signals (ADCP velocity time series, stretches of relevant time series, and video-derived quantities that are $15 - 20[min]$ long). Continuous Wavelet Transforms (CWT) were computed using a Morse wavelet (e.g., Lilly and Olhede, 2012; Hlawatsch and Auger, 2013; Martinez-Ríos et al., 2022), and were applied to longer time series to identify time-variations in the dominant frequencies.

3.2.3 Momentum balance

The cross-shore depth-averaged momentum equation for steady state, hydrostatic flow, and small sea level variations —neglecting the Coriolis force— is shown in Equation 3.2.

$$\underbrace{\frac{1}{h}\frac{\partial}{\partial x}\int_{-h}^{0} u^2 dz}_{(1)} + \underbrace{\frac{1}{h}\frac{\partial}{\partial y}\int_{-h}^{0} uv dz}_{(2)} = -\underbrace{\frac{1}{\rho_0}\frac{\partial P}{\partial x}}_{(3)} - \underbrace{\frac{\tau_{bx}}{\rho_0 h}}_{(4)} - \underbrace{\frac{1}{\rho_0 h}\frac{\partial S_{xx}}{\partial x}}_{(5)} \tag{3.2}$$

Advection (2), pressure gradient (3) and bottom stress (4) are neglected to consider only a balance between outflow momentum (1) and wave induced momentum (5) (e.g., Rodriguez et al., 2018; Kastner et al., 2019).

Following Rodriguez et al. (2018) and Kastner et al. (2019) we calculated the river and wave momentum fluxes to evaluate the potential of freshwater to escape the surfzone. The river momentum flux was estimated as $\rho U_0 Q/b_m$, where ρ is the density of water, U_0 is a representative velocity at the river mouth, Q is the river discharge and b_m is the cross-section width at the mouth. River velocity U_0 at the mouth was computed using the ADCP measurements, estimates of the cross-sections at point A and the outflow channel, and the assumption of constant discharge between these cross-sections (Figure 3.1a). The widths of these cross-sections were estimated based on drone footage. The water depth at the ADCP cross-section was estimated based on the ADCP backscatter, the bottom CTD at point A and the pressure sensor at point C, whereas for the outflow channel the depth was defined based on CTD profiles taken at the river mouth. The cross-sectional shapes were defined parabolic based on width and depth estimations. Depth-averaged velocity was calculated from the raw ADCP data and then integrated over the cross-section to estimate Q. The representative velocity U_0 was then estimated using Q and the continuity equation.

The cross-shore (S_{xx}) and oblique (S_{yx}) components of the wave radiation stresses (wave momentum flux) were calculated as Equations 2.19 and 2.21 (e.g., Longuet-Higgins and Stewart, 1962, 1964). Wave heights measured at $h = 20[m]$ (from the ADCP at San Antonio's Port) are propagated shoreward to the breakpoint using linear wave theory and the breaker index criteria (γ) proposed by Battjes (1975) (Equation 2.16).

For wave propagation, the beach slope is assumed to be constant and equal to 0.01. The oblique component of the wave radiation stress is used here as a proxy of alongshore currents (e.g., Longuet-Higgins, 1970), which may contribute to freshwater trapping and alongshore transport in the surfzone (e.g., Grant et al., 2005; Wong et al., 2013).

Chapter 4

Results

4.1 Field Conditions

River discharge at the upstream gauging station slowly decreased from $27 - 20[m^3/s]$ throughout the field campaign. Offshore wave heights and peak wave periods varied from $1 - 3[m]$ and $10 - 14[s]$, respectively (Figure 4.1d). Offshore wave direction θ remained almost invariant with a mean value of 16° (waves from the southwest). Tides in the area are mixed semi-diurnal, with maximum (minimum) tidal range of $1.7[m]$ ($1.2[m]$) during our field campaign (Figures 3.1c and 4.1e).

Inlet and plume dynamics are strongly modulated by the tide (Figure 4.1). The depth-averaged along channel velocities at point A in the inlet (Figure 3.1a) reach a maximum of $1[m/s]$ during the ebb (Figure 4.1c). The along channel velocity switches direction with the tide, with oceanward (positive) flow during ebb and landward (negative) flow during the flood. Surfzone salinity at the river mouth ($SZ1$ mooring) indicates that a freshwater plume formed only during ebb tides as freshwater leaves the estuary (Figure 4.1a,c,e). During the flood, surfzone salinity at $SZ1$ rapidly increases to ocean values (Figure 4.1a,e). Surfzone salinity at $SZ2$, located $\sim 200[m]$ north of $SZ1$ (Figure 3.1a), indicates that freshwater does not reach this location at all tidal cycles; salinity remains at ocean salinity values during the first three days of the campaign (Sept 05-07). After Sept 07, surfzone salinity at $SZ2$ shows tidal variability with the presence of freshwater on ebb tides, although on average, salinity values are much higher than at $SZ1$ during ebb tides.

Surfzone CTD time series are clearly different to each other. Point $SZ1$ measures salinity values from seawater at high tide to freshwater at low tide (Figure 4.1a), whereas point $SZ2$ only reaches brackish water salinity values at low tide (Figure 4.1b). This difference between time series depending on instrument location is explained by different plume dynamical regions (Horner-Devine et al., 2015) such us near-field, mid-field and background seawater. Furthermore, analysing $SZ2$ salinity time series we observe that during the first 36 hours the sensor measures seawater most of the time, with sporadic low salinity peaks. Afterwards, and for the rest of the study, $SZ2$ CTD measurements are also modulated by the tide, with mixed water values at low tide.

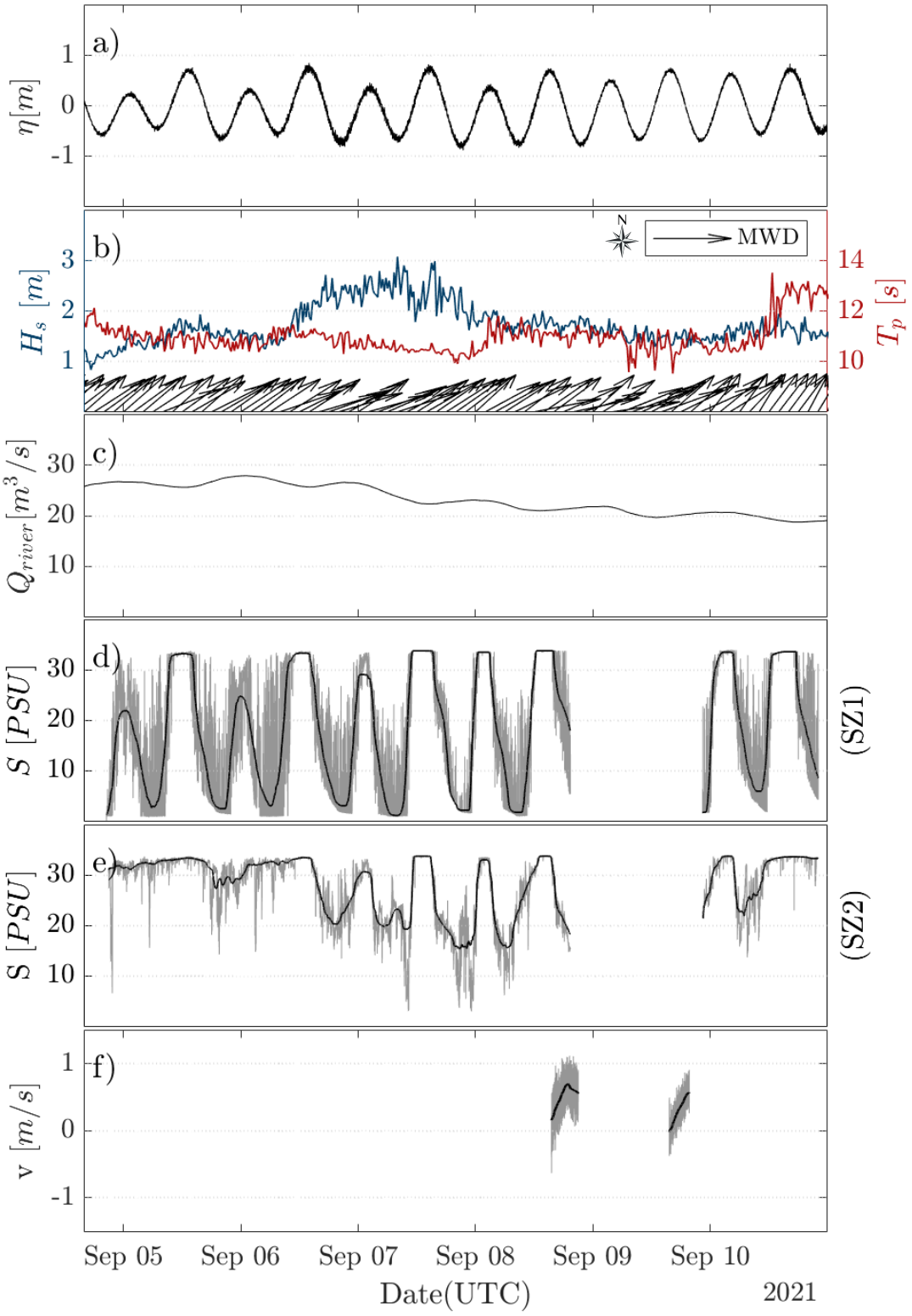

Figure 4.1: Collected Data. (a) Tidal elevation at Port of San Antonio. (b) Wave climate; significant wave height (blue), peak period (red) and mean wave direction (black arrows). (c) River outflow at Cabimbao station. (d,e) Salinity at locations $SZ1$ and $SZ2$, respectively. Dark lines show a moving median whereas raw data are shown in light gray. (f) Depth-averaged velocity at location L, mean of $10[s]$ (gray) and $1[h]$ (black).

4.2 Inlet-Plume Oscillations

The salinity signal in the surfzone, and the pressure and velocity signals in the inlet show strong oscillations on top of the tidally-induced variations (e.g., Figure 4.2a,b,f). Surfzone salinity $(SZ1)$ presents persistent low frequency oscillations that have amplitudes on the order of $10 - 15[psu]$, with maximum values reaching $25[psu]$ during low tide conditions (Figure 4.2a). Surface elevation in the inlet shows similar low-frequency oscillations with amplitudes of $30[cm]$ (Figure 4.2b). The oscillations in both salinity and surface elevation are modulated by the tide; for salinity, the amplitude of the oscillations increases as the tidal elevation decreases, with maximum amplitudes around low tide, whereas the oscillations of surface elevation are maximum during high tide, and decrease in amplitude as the ebb progresses (Figure 4.2 a,b).

The wavelet spectra show that the oscillations observed in surfzone salinity and inlet water levels are associated with infragravity (IG) wave motions in the nearshore, as most of the spectral energy is found for periods between $30[s] - 5[min]$ and with a temporal evolution that is consistent with the tidal variability (Figure 4.2c,d). The periods of greater spectral energy in surfzone salinity and inlet water levels do not overlap completely; we note that during the early ebb both salinity and water elevation show significant spectral energy in the IG band, whereas significant spectral energy in the IG band is only evident in the surfzone salinity signal during the late ebb. This is coherent with IG wave energy being mostly blocked from propagating into the inlet (Figure 4.2b,c,d).

Oscillations in the IG frequency band are also observed in flow velocity during the early ebb (Figure 4.2e,f), with a strong peak in power spectral density at a period of $250[s]$. After the maximum along-channel velocity is reached, i.e., late ebb, the spectral energy contained in the IG band decreases, which is similar to what is observed for inlet water levels (Figure 4.2b,d). However, small peaks are still identifiable in the PSD of along channel velocities at IG periods during the late ebb (Figure 4.2e).

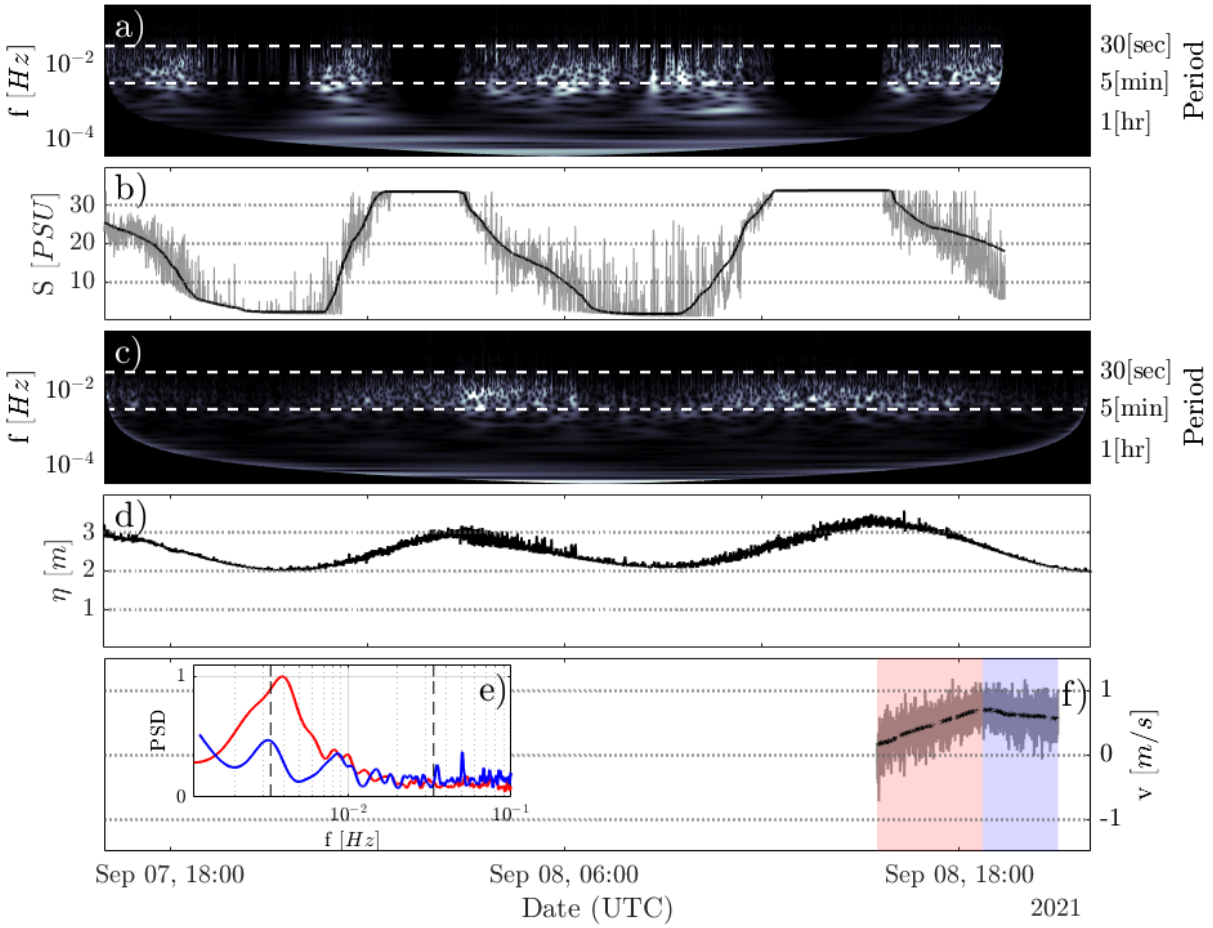

Figure 4.2: Time-frequency Analysis of a Tidal Cycle. (a, c) Wavelet transform and (b, d) time series of salinity at $SZ1$ and water elevation at A, respectively. (e) PSD and (f) time series of depth-average velocity at L with a moving mean of $10[s]$ (black) and $1[h]$ (grey). PSD calculated with $15[min]$ windowing, for first and second half of the ebb in red and blue, respectively, matching shaded areas in panel (f).

4.3 Plume response

As mentioned in Section 4.1, the presence of a plume in the surfzone is modulated by the tide, with freshwater leaving the estuary during the ebb. Consequently, plume response is analysed only for that tidal stage.

As shown in Figures 4.1 and 4.2, the freshwater plume only forms during ebb tides in the Maipo system under low river discharge conditions. Consequently, plume formation and response to the nearshore wave forcing are analysed only for the ebb, which we divide into an early and late ebb periods following the clear differences in salinity, velocity and water levels that are observed as the tidal elevation drops from high to low tide. (Figures 4.1 and 4.2).

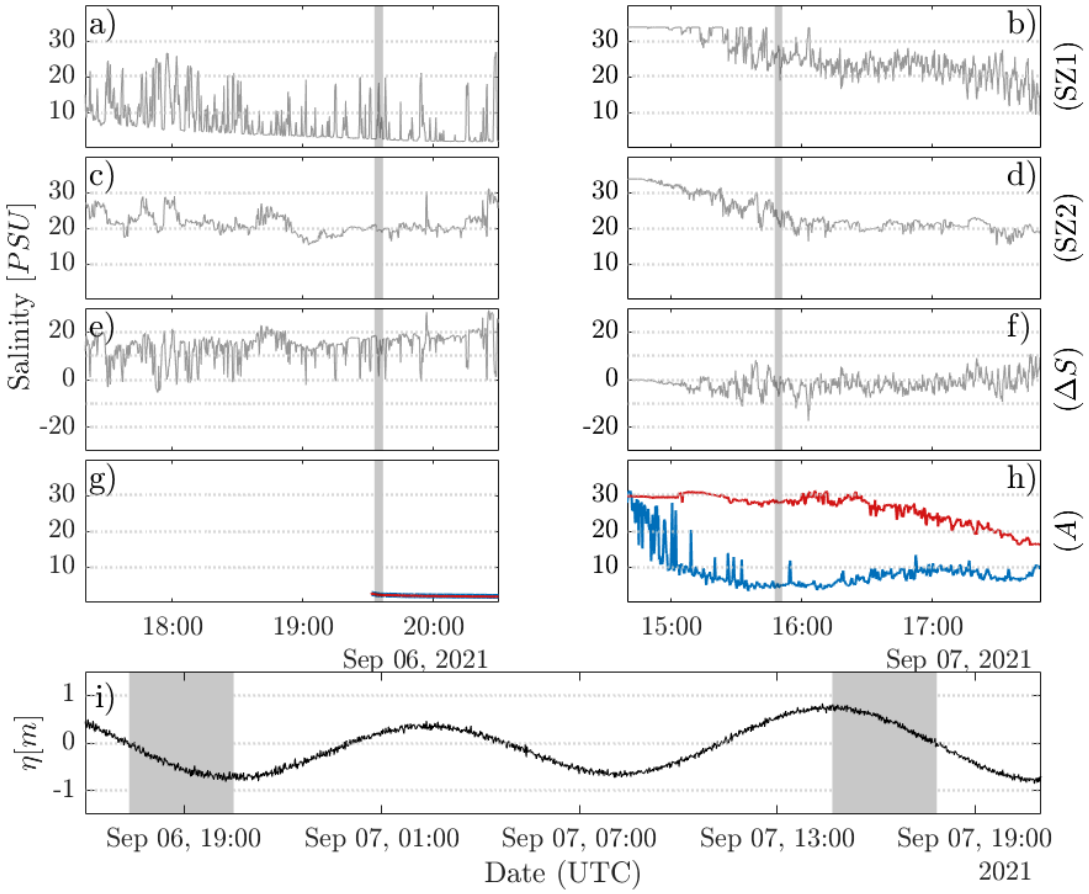

Figure 4.3: Plume Response, Salinity Signals. Salinity at $SZ1$ (a,b) and $SZ2$ (c,d). (e,f) Salinity difference between locations $SZ2$ and $SZ1$. (g,h) Salinity at point A, surface in blue and bottom in red. Left and right side panels show late-ebb and early-ebb periods, respectively as shown in panel (i) with grey shaded areas. Panels (a,c,e,g) and (b,d,f,h) show drone footage of Figure 4.5 and 4.4, respectively, in grey shaded area.

Figure 4.3 shows salinity at $SZ1$ and $SZ2$, and top-bottom salinity at point A in the inlet for a late ebb period (left panels) and an early ebb period (right panels). These periods were chosen based on the availability of drone imagery documenting the surfzone and near-field river plume. The salinity at moorings $SZ1$ and $SZ2$ decreased from ocean water values ($\sim 32[psu]$) to approximately $20[psu]$ during the early-ebb (Figure 4.3b,d).

The salinity at $SZ1$ and $SZ2$ follow a similar pattern overall, such that their difference oscillates around $\Delta S \sim 0$ (Figure 4.3f). However, $SZ1$ shows higher variability and larger oscillations (Figure 4.3b,d). Salinity in the inlet shows large stratification during the early ebb, with top-bottom salinity differences reaching $20[psu]$ (Figure 4.3h). Stratification decreases slowly during the early ebb as salty water progressively leaves the estuary (Figure 4.3h).

During the late-ebb (left panels in Figure 4.3), the salinity signals at $SZ1$ and $SZ2$ differed considerably in terms of magnitude and variability; $SZ1$ showed values that are generally less than $10[psu]$, but with large oscillations (amplitude of $\sim 15 - 20[psu]$), whereas $SZ2$ presented low variability and $S \sim 20[psu]$ (Figure 4.3a,c). The differences in salinity between $SZ1$ and $SZ2$ are evident in Figure 4.3e, where ΔS fluctuated around $10 - 20[psu]$. Salinity data in the inlet during the late ebb showed an outflow of freshwater ($S \sim 0$) with no vertical stratification (Figure 4.3g). Although salinity data in the inlet is not complete for the selected late-ebb time window (Figure 3.1d and Figure 4.3g), the vertical salinity structure showed no stratification throughout the late ebb during our deployment as confirmed by the same instrumentation in different periods and by kayak-based salinity profiles at the same tidal stage (not shown).

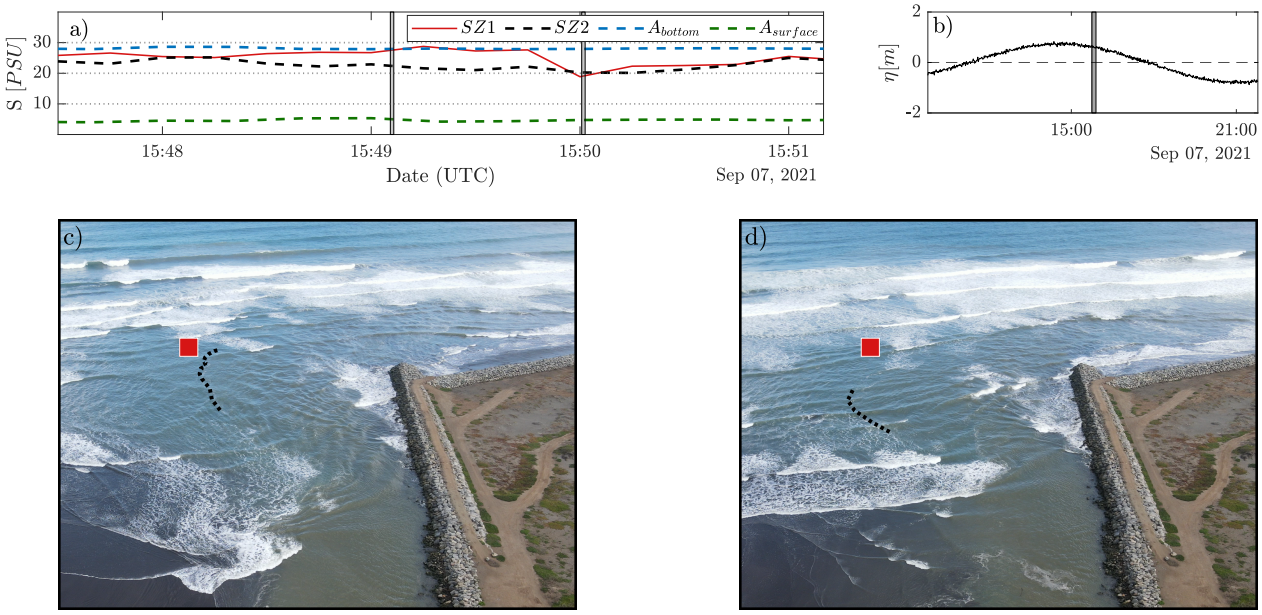

Figure 4.4: Early-ebb Plume Response. (a) Evolution of salinity at $SZ1$ (red curve), at surface inlet (bottom green dashed line), at bottom inlet (upper blue dashed line) and at $SZ2$ (middle black dashed line). (b) Tidal stage of drone footage. (c, d) Drone snapshots of the river mouth at different times according with vertical lines in (a). The red square highlights $SZ1$ CTD location and black dotted line remarks (NDTI identifiable) plume front.

Drone flights capturing the near-field plume and surfzone region (including sensor $SZ1$) documented the plume response to the nearshore wave forcing and contextualise the in-situ salinity measurements (Figures 4.4 and 4.5). During the early-ebb, the salinity at $SZ1$ oscillated between $\sim 20 - 30[psu]$ (Figures 4.3b and 4.4a), as the plume developed constrained to the jetty (Figure 4.4c,d). At this time, water levels were high (Figure 4.4b) and waves propagated into the river mouth and inlet (Figure 4.4c,d). Infragravity bores were frequently observed to propagate upstream in the outflow channel (e.g., Figure 4.4c), which is consistent with observations of IG energy in surfzone salinity, and water levels and velocity signals in the inlet (Figure 4.2c,d,e). Surfzone salinity at $SZ1$ oscillated between the values observed at $SZ2$ and the salty ocean water

observed in the near-bed at location A in the inlet (Figure 4.4a). This indicates that i) the $SZ1$ mooring recorded the presence/absence of the plume as the edge of a weekly developed near-field plume moves in response to incident waves (Figure 4.4a,c,d), and ii) plume water is likely transported north upon exiting the estuary reaching the $SZ2$ mooring.

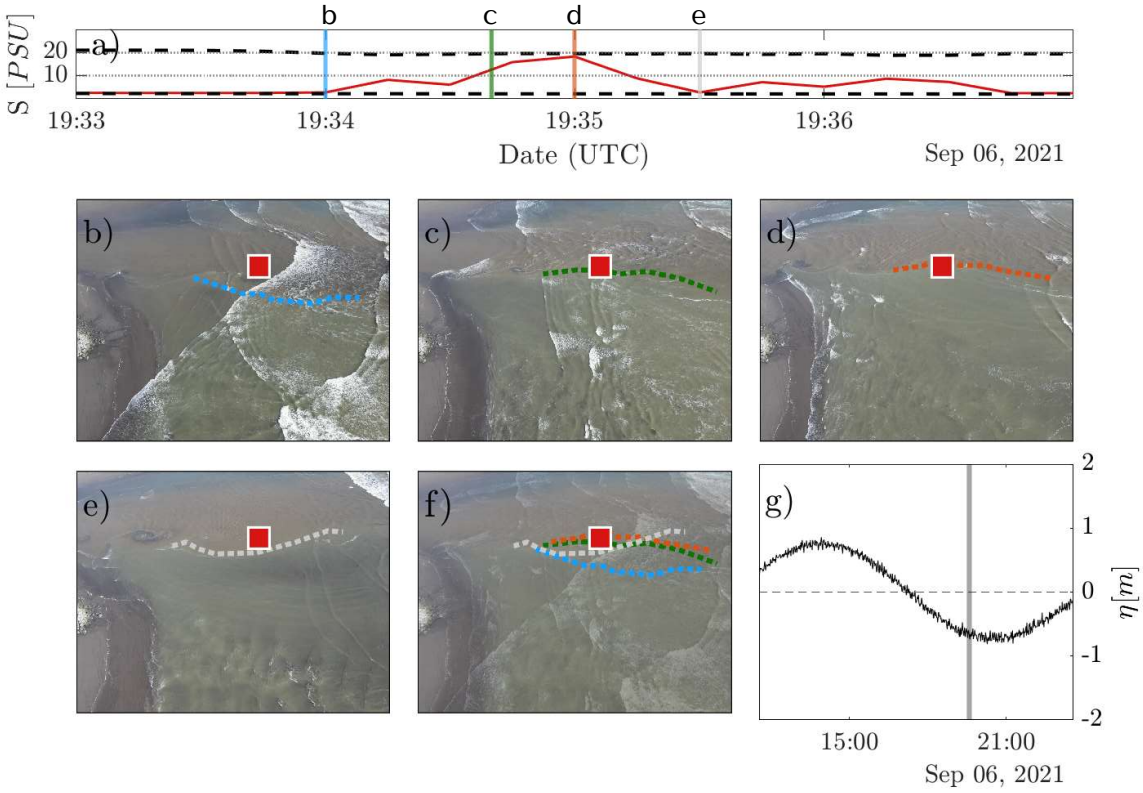

Figure 4.5: Late-ebb Plume Response. (a) $SZ1$ salinity in red; upper and bottom dashed lines show salinity in the surface inlet and at $SZ2$, respectively. (b, c, d, e) Snapshots of the mouth, red square highlights $SZ1$ CTD location and colour dotted line remarks (NDTI identifiable) plume front. Time of the snapshots indicated in panel (a) with colour matching shaded vertical lines. (f) Average image of the snaps with all the plume front lines. (g) Tidal stage of drone footage.

During late-ebb, the plume developed into a strong outflow turbid jet as the tide retreated and the water level dropped (Figure 4.5). The salinity oscillations at $SZ1$ (Figure 4.3a and Figure 4.5a) combined with drone observations show that the freshwater jet contracted and expanded such that the $SZ1$ mooring was periodically in and out of the plume (Figure 4.5a-f). Figure 4.5b-e show consecutive snapshots (at times indicated in Figure 4.5a) of the plume jet where the plume edge, as identified by the NDTI threshold, was observed to expand and contract in coherence with the salinity signal at $SZ1$ (Figure 4.5a). The first snapshot (Figure 4.5b) shows that the $SZ1$ mooring was in the plume; at this time, $SZ1$ showed $S \sim 0[psu]$ (Figure 4.5a). Later, the plume contracted such that the plume edge was progressively closer to $SZ1$ and eventually moved farther (Figure 4.5c,d), which is reflected in an increase in salinity (Figure 4.5a). Finally, the plume expanded such that $SZ1$ is located inside the freshwater jet (Figure 4.5a,e).

Chapter 5

Discussion

5.1 Surfzone-inlet IG oscillations

The salinity signal in the surfzone ($SZ1$) varied in response to the tide; the river plume only formed during the ebb during these low discharge conditions (e.g., Figures 4.1 and 4.2). Large low-frequency persistent oscillations are observed in surfzone salinity and inlet water surface levels on top of the tidally-induced variations, which occur primarily at IG wave frequencies (Figure 4.2a,b,c,d). Fluctuations at IG frequencies were also observed in inlet velocity (Figure 4.2 e,f). These results confirm that the influence of the nearshore infragravity wave forcing is felt throughout the Maipo surfzone-inlet system, which is coherent with the observations reported by Flores et al. (2022).

The observed salinity and plume patterns in the surfzone result from the continuous interaction of surfzone and estuarine hydrodynamics. While IG wave motions exist offshore (e.g., Reniers et al., 2010, 2021), they are strongest near the shoreline (e.g., Guza and B. Thornton, 1985; Elgar et al., 1992), and are frequently associated with the onset of depth-limited breaking of wave groups and nonlinear interactions in the incident short waves (e.g., Symonds et al., 1982; Schäffer, 1993). Unlike the short wave forcing, IG waves released in the surfzone are observed to travel shoreward and propagate upstream in small estuaries and tidal inlets inducing large velocity and water level fluctuations (e.g. Dodet et al., 2013; Williams and Stacey, 2016; Melito et al., 2018; Flores et al., 2022).

Time-frequency analysis of surfzone salinity and inlet water levels shows that the observed plume patterns (salinity) are modulated by the tide, and suggests a disconnection of the inlet-surfzone system during the late ebb as energy in the IG band exists in surfzone salinity but not in the inlet water levels and flow velocity (Figure 4.2). Consequently, salinity and plume oscillations during the late ebb would be forced primarily by surfzone processes, with little o no influence of IG modulations in the inlet (Figure 4.2 and Figure 4.5). In this shallow system, wave blocking (e.g. Bertin and Olabarrieta, 2016; Bertin et al., 2019) may occur due to bathymetric features at the mouth (e.g., Williams and Stacey, 2016) and by supercritical ebbing currents in the outflow channel (e.g., Dodet et al., 2013). Although we cannot evaluate all the mechanisms generating partial or total blocking of IG motions in the Maipo estuary, we do observed supercritical currents in the outflow channel and near-field plume during the late ebb phase, as seen in drone snapshots (Figure 4.5). The wavelet spectra (Figure 4.2) suggests that the salinity and plume oscillations result from a combination of surfzone and inlet processes during the early ebb. This is evidenced from the energy in the IG band in both surfzone salinity and inlet water levels (Figure 4.2c,d).

5.2 Wave groups processes

The generation mechanisms of IG waves (and energy) in the nearshore are primarily associated to the presence of wave groups in the incident short wave forcing (e.g., Longuet-Higgins and Stewart, 1962; Symonds et al., 1982; Bertin et al., 2018). Deep water waves travel in groups (Svendsen, 1984; O'Connor et al., 1999; Bertin et al., 2018), and as they approach onshore and break, IG waves are generated via the bound wave release (Longuet-Higgins and Stewart, 1962) or the moving breakpoint generation mechanisms (Symonds et al., 1982; Schäffer, 1993). The latter is associated with time variations in the location of the breakpoint as larger waves break further offshore than smaller waves, generating time variations of the radiation stress gradients and the wave-induce setup (e.g. Symonds et al., 1982; Contardo and Symonds, 2013).

Time variations of the cross-shore location of the breakpoint can be readily identified with drone footage (e.g., Moura and Baldock, 2017; Flores et al., 2022), which we used as a proxy for the arrival of wave groups and the generation of infragravity wave forcing in the surfzone (Figure 5.1a,b).

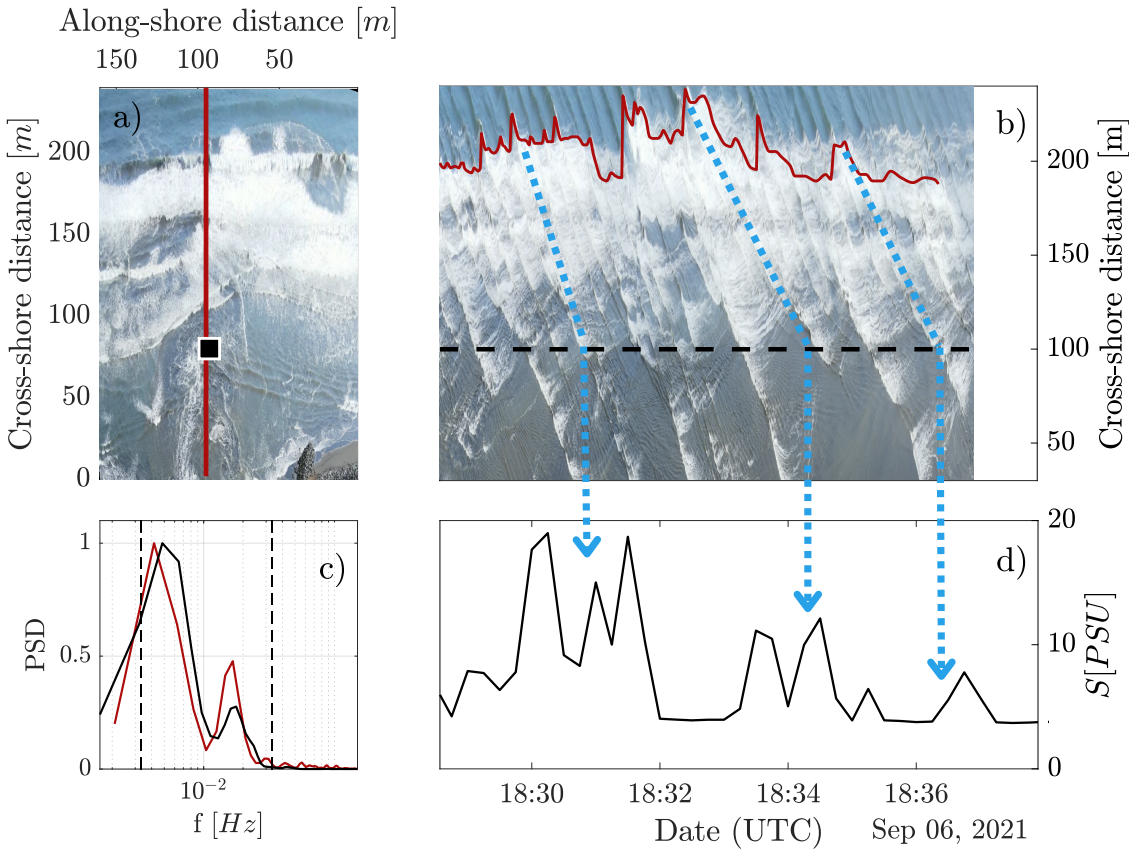

Figure 5.1: Wave-Plume Interaction at Wave Groups (IG) time scales. (a) Example of rectified frame of drone footage; red vertical line indicates alongshore coordinate for timestack and black square shows the $SZ1$ CTD location. (b) Timestack of the surfzone where the red line highlights the breakpoint and the black dashed line shows the $SZ1$ CTD location. (c) PSD of timestack-derived breakpoint signal and $SZ1$ salinity, in red and black, respectively. (d) $SZ1$ salinity signal. Blue dotted arrows remark breakpoint offshore shifts, follow wave front (oblique) to the $SZ1$ CTD location and indicate its measurement in panel (d).

Figure 5.1b shows a cross-shore timestack (time-space map) derived from a rectified drone flight at the alongshore coordinate of sensor $SZ1$ (indicated by the red line in Figure 5.1a), where the variability in the location of the breakpoint (red line, extracted using a pixel intensity threshold method) is identified; an offshore (onshore) shift of breakpoint location implies larger (smaller) wave groups arriving and breaking.

We observed a strong correlation between breakpoint location, and the arrival of wave groups, and surfzone salinity at $SZ1$ (Figure 5.1b,c,d). In particular, we observed that i) salinity at $SZ1$ increased when waves were higher and the breakpoint shifted offshore (Figure 5.1b,d), and ii) the frequency spectra of breakpoint location and salinity time series were similar, showing peaks at the same frequencies in the infragravity frequency band (Figure 5.1c). These observations strongly suggest that oscillations in surfzone salinity at the river mouth result from the variability in the wave forcing associated to wave groups during periods of low river discharge.

5.3 Wave-curent interaction processes

Wave-current interaction is an important process for the dynamics of coastal zones, especially in estuaries and tidal inlets where the outflow river currents oppose shoreward wave propagation (e.g., Olabarrieta et al., 2011, 2014; Jia et al., 2015; Chen et al., 2019). The opposition by river currents causes a Doppler shift on wave frequency ω (e.g., Zippel and Thomson, 2015),

$$\omega = \sqrt{gk\tanh(kh)} + \vec{u}\cdot\vec{k} = \omega_0 + \Delta\omega \tag{5.1}$$

where ω_0 is the intrinsic wave frequency, which follows the dispersion relation, and the frequency shift $\Delta\omega$ depends on the current velocity $\vec{u}$ and wavenumber $\vec{k}$. As wave frequency is constant, an opposing current results in a decrease in wavelength and celerity (e.g., Peregrine, 1976; Thomas, 1981).

Our observations of river-wave dynamics in the surfzone show that wave-current interaction results in wave fronts that bend and refract in response to the opposing river outflow currents, particularly during the late ebb (Figure 4.5). The wave fronts refract and become steeper as waves propagate shoreward and interact with the plume jet.

The outflow jet current $\vec{u}$ and wave propagation $\hat{k}$ have opposite directions, which results in a decrease in wave celerity and wavelength in the plume area (e.g., Peregrine, 1976; Thomas, 1981). Similar to refraction due to changes in water depth as obliquely incident wave fronts propagate shoreward, the changes in celerity along wave fronts due to opposing currents cause wave refraction; the parts of the wave front toward the edges of the plume and outside the jet move faster as the influence of opposing currents decrease (e.g., Figure 4.5b,f). Bathymetric features such a discharge channel may reduce this effect, however, it is clear that the effect of opposing currents dominates in this site (Figure 4.5b,f). Figure 5.2 depicts the wave-current interaction phenomena explained above.

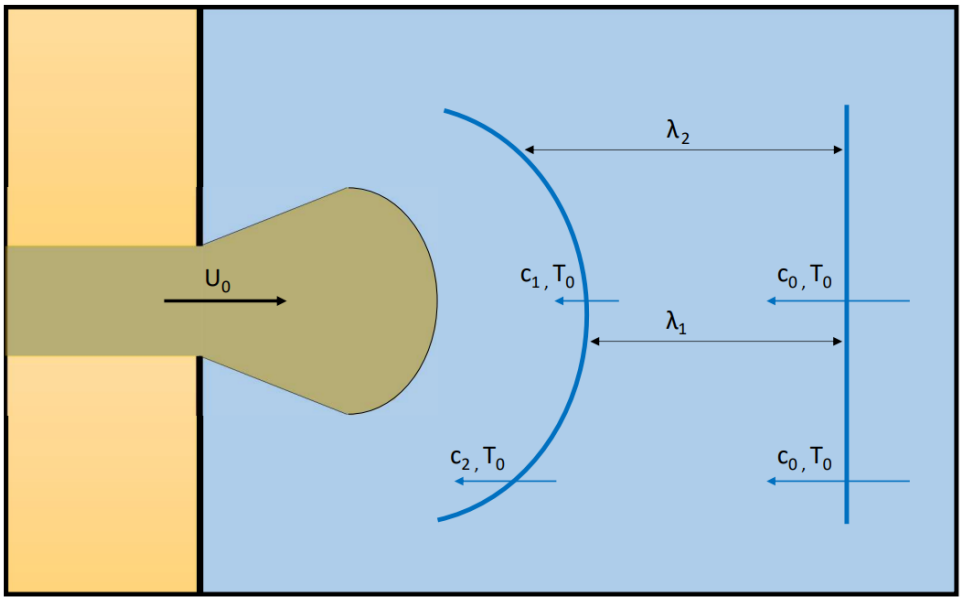

Figure 5.2: Wave Bending due to Wave-Current Interaction with the river outflow.

5.4 Proposed physical mechanism

The propagation and breaking of wave fronts in the plume area, which occurs at the timescale of wave groups, may generate the IG band oscillations in surfzone salinity (Figure 4.2a,c).

We hypothesise that the onshore directed wave force exerted by breaking waves propagating obliquely in the plume area due to refraction by wave-current interactions (e.g., Figure 4.5b) forces plume water inward (relative to its axis) and contributes to the contraction of the plume jet (e.g., Figure 4.5c).

As the intensity of the wave forcing reaching the near-field plume area is modulated by the arrival of wave groups, the contraction and expansion of the jet should occur at infragravity frequencies; the jet contracts when larger waves reach the mouth area and expands (or relaxes) when low amplitude waves arrive.

Although this mechanism explains the variability observed in our surfzone salinity measurements and is plausible based on the combined analysis of drone and in-situ observations, further research is required to quantify the dynamical balance at the river mouth and evaluate its prevalence.

We note that these observations align with those of Flores et al. (2022) at the same site, which reported a cross-shore modulation of the far-field plume edge at infragravity time scales by variability in the wave-driven circulation associated to wave groups.

5.5 Plume Retention and Escape

Recent studies have shown that the nearshore wave forcing and wave breaking in the surfzone impact the structure of small plumes, limit their cross-shore spreading and contribute to trap river water near the coastline (e.g., Delpey et al., 2014; Rodriguez et al., 2018; Kastner et al., 2019; Moghimi et al., 2019; Kastner et al., 2022; Flores et al., 2022).

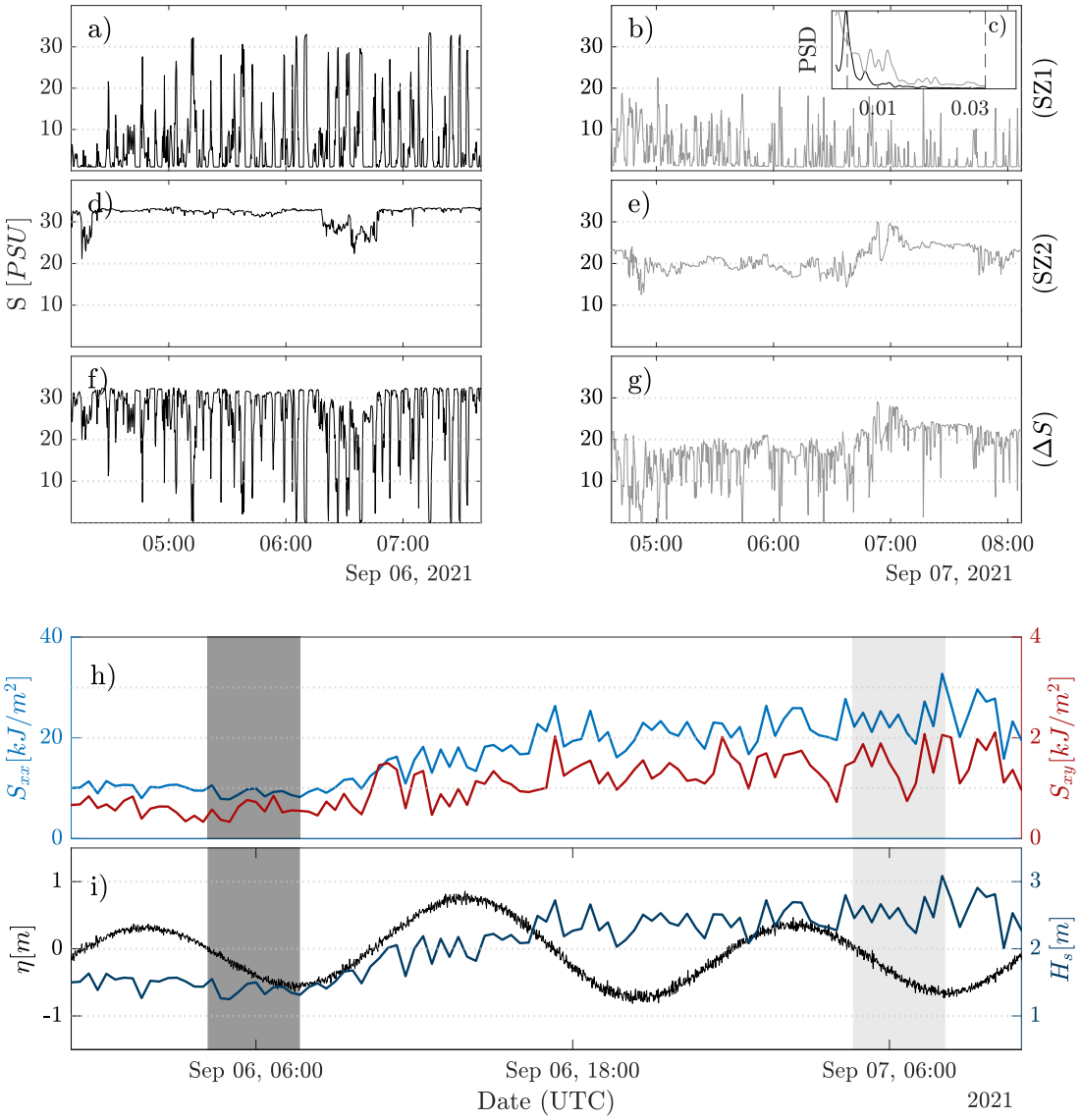

Figure 5.3: Wave Climate Influence in Late-ebb Plume Response. (a,b) Salinity at $SZ1$ and (c) PSD of both signals matching colours. (d,e) Salinity at $SZ2$. (f,g) Salinity difference between $SZ2$ and $SZ1$. Left (a,d,f) and right (b,e,g) panels show data for low and high wave forcing, respectively. (h) Cross-shore and alongshore components of radiation stress calculated offshore, in blue and red, respectively. (i) Tidal elevation and offshore significant wave height in black and blue, respectively. Dark and light grey shaded areas in panels (h,i) indicate time of data showed in panels (a,d,f) and (b,e,g), respectively.

Surfzone measurements ($SZ1$ and $SZ2$) agree with these studies as they showed synoptic variability suggesting that freshwater content in the surfzone responds to the observed wave conditions (e.g., Figure 5.3). Figure 5.3 shows clear differences in surfzone salinity for two late ebb periods on Sept 06 and 07 that experience wave forcing of varying intensity and similar river discharge conditions. While surfzone salinity at $SZ1$ shows to be greatly influenced by oscillations in the IG band on both days (Figure 5.3a,b,c), the amplitude of these oscillations is much greater on Sept 06, which shows smaller offshore significant wave height (Figure 5.3a,i) and radiation stresses (Figure 5.3h) than Sept 07.

As shown in Figure 4.5, the $SZ1$ mooring is periodically in and out of the plume during the late ebb, and larger salinity oscillations (reaching $\sim 30[psu]$ on Sept 06) suggest that freshwater content outside of the outflow jet is lower (Figure 5.3a).

Differences in surfzone salinity between these two days are even more evident at mooring $SZ2$ (Figure 5.3d,e); on Sept 06, with smaller wave height and forcing, $SZ2$ largely shows salinity corresponding to ocean values as the jet likely punches through the surfzone, whereas on Sept 07 (higher wave forcing) salinity at $SZ2$ persistently shows the presence of freshwater, with salinity typically in the range of $18-25[psu]$ (Figure 5.3d,e,h,i).

We interpret these differences in salinity with varying wave forcing conditions, primarily those observed in $SZ2$ located $\sim 200[m]$ north of the river mouth, as the plume (and freshwater) mostly trapped in the surfzone when salinity at $SZ2$ is low and waves are high, and a great fraction of the freshwater input escaping the surfzone when salinity at $SZ2$ is high and offshore wave climate is low. Figure 5.4 schematises the plume escape/retention interpretation via surfzone CTD measurements described above.

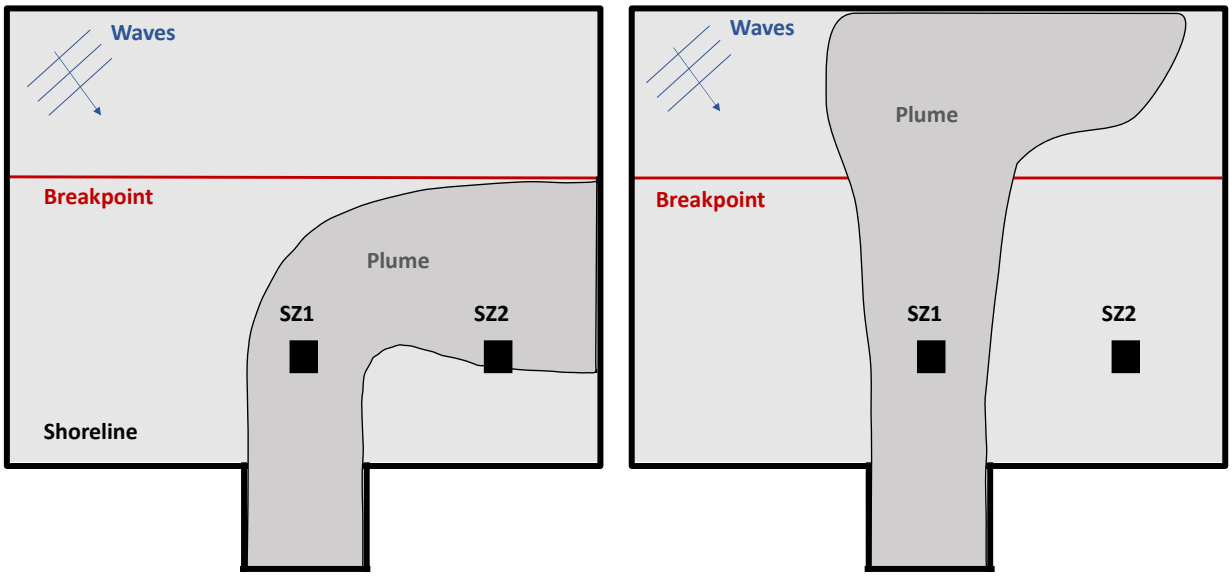

(a) Plume retention (b) Plume escape

Figure 5.4: Plume Escape and Retention Identification via Surfzone CTDs. (a) Plume trapped in the surfzone scenario, with sensor $SZ1$ located in the jet trajectory and sensor $SZ2$ located in a mid-field region. (b) Plume escaping the surfzone scenario, with sensor $SZ1$ located in the jet trajectory and sensor $SZ2$ located in seawater.

We use the momentum balance approach of Rodriguez et al. (2018) to further assess the potential for waves to trap freshwater in the surfzone. We compare the onshore shore-normal wave momentum flux S_{xx} at breakpoint to the offshore river momentum flux at the mouth (see Section 3.2.3); large part of the freshwater input is expected to escape the surfzone when river momentum exceeds the incident wave momentum, whereas most part of the freshwater input is entrained into the surfzone when the opposite occurs (e.g., Rodriguez et al., 2018; Kastner et al., 2019).

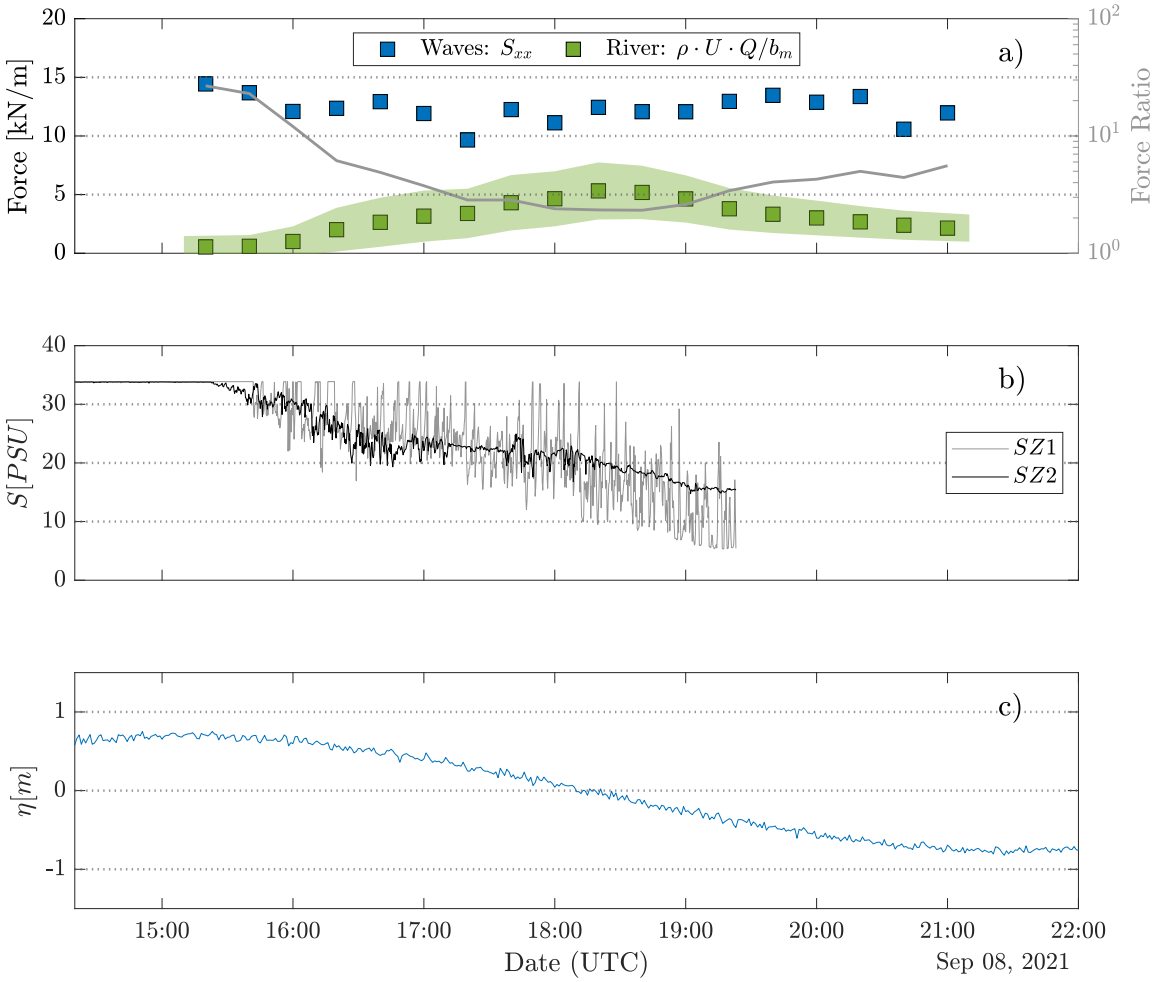

Figure 5.5: Wave-River Momentum Balance. (a) Force per width unit. Wave induced force (blue) is calculated with cross-shore radiation stress component (S_{xx}) at the breakpoint. River force (green) is calculated with depth averaged ADCP velocity measurements with a moving average of $1[h]$ and transformed to the velocity at the mouth. Green shaded area indicates a range for the river force considering variability in velocity measurements (i.e., not moving average). (b) Salinity at points $SZ1$ and $SZ2$ in grey and black, respectively. (c) Tidal elevation at San Antonio port.

Figure 5.5 shows the wave and river momentum terms for an ebb tide period on Sept 08 (when inlet velocity data is available, see Figure 4.1), along with surfzone salinity at $SZ1$ and $SZ2$. We observe that the wave force is much greater than the river force, with a wave/river force ratio reaching a minimum of ~ 2 towards mid-ebb as inlet velocities reach a maximum (Figure 4.2f and 5.5a). On this day, the momentum ratio suggests

that a large percentage of freshwater remains in the surfzone (e.g., Rodriguez et al., 2018), which is consistent with the surfzone salinity observations at $SZ1$ and $SZ2$ showing the presence of freshwater (Figure 5.5b).

Both the river velocity and wave forcing present variability at short time scales (e.g., Figure 4.2), which are not included in the momentum scaling presented above. In this system, variability associated to the infragravity wave forcing, i.e, wave groups, seems to be main source of variability a time scales less than 5 min (Figure 4.2). It is likely that variability at infragravity frequencies causes rapid changes in the dynamical balance between the wave and river forcing. In the contraction and expansion mechanism discussed above, for example, a contraction of the plume jet would result in flow acceleration and and increase in outflow velocity, likely increasing river outflow momentum that may result in a greater percentage of river water escaping the surfzone. The feasibility and importance of these potential effects should be studied in the future to further assess what timescales are relevant to freshwater export in small river systems.

Chapter 6

Conclusions

In this study we used in-situ data and drone imagery to investigate interactions between the outflow plume and the nearshore wave forcing at the mouth of a small-scale river system. We find that these interactions are modulated by the tide, as i) the freshwater plume only forms during the ebb, and ii) the dynamics of interactions change as the ebb progresses and a strong outflow jet develops. Therefore, the second hypothesis is corroborated.

On timescales less than a tidal cycle, variability in salinity, water levels and velocity is controlled by infragravity motions, which are felt throughout the inlet-surfzone system. These motions are largely blocked from propagating into the inlet during the late ebb, suggesting that observed plume variability is controlled by surfzone processes. The combined analysis of surfzone salinity and drone imagery suggests that wave groups, and the time variability in wave forcing associated to their arrival, result in an expansion/contraction of the plume at the mouth. Thus, the first hypothesis is partially confirmed, since plume hydrodynamics are influenced at infragravity timescales but wave groups are responsible for these motions and not specifically the propagation of infragravity waves.

On time scales larger than a tidal cycle, we find that surfzone salinity responds to the incident wave forcing, as a more intense wave climate (wave heights, S_{xx}, S_{xy}) generally results in lower salinity at our two moorings, suggesting that a large percentage of freshwater is confined near the coast. Results we not conclusive to assess the third hypothesis. Nevertheless, these observations agree with previous studies highlighting the potential for nearshore waves to prevent the offshore expansion of plume waters. Overall, we find that nearshore waves influence near-field plume dynamics and outflow pathways of river water at infragravity timescales, associated to the arrival of wave groups, and at longer timescales related with the synoptic variability of the offshore wave forcing.

The findings of this work allow us to set basis for a new hypothesis. We hypothesise that wave-river interaction at IG time scales may influence the final destination of small-scale rivers freshwater in the coast. As the results of this work show, the simplified momentum balance for the study site indicates that both, river discharge and nearshore wave forcing are quite similar in magnitude for a low river discharge scenario. Coupling this statement with the influence of wave groups on plume dynamics, which inputs variability to wave induced momentum, we expect that smaller waves within a groups may imply transient freshwater escapes from the surfzone for a trapped plume scenario where river and wave momentum are similar.

The link between short time scale dynamics and the previous synoptic approaches (e.g., Wong et al., 2013; Rodriguez et al., 2018; Kastner et al., 2019) to assess plume waters final destination is a certain research focus for future work.

Bibliography

J. M. Barragán and M. De Andrés. Analysis and trends of the world's coastal cities and agglomerations. *Ocean & Coastal Management*, 114:11–20, 2015.

N. Basdurak and J. Largier. Wind effects on small-scale river and creek plumes. *Journal of Geophysical Research: Oceans*, 127(12):e2021JC018381, 2022.

N. Basdurak, J. Largier, and N. Nidzieko. Modeling the dynamics of small-scale river and creek plumes in tidal waters. *Journal of Geophysical Research: Oceans*, 125(7):e2019JC015737, 2020.

J. Battjes and M. Stive. Calibration and verification of a dissipation model for random breaking waves. *Journal of Geophysical Research: Oceans*, 90(C5):9159–9167, 1985.

J. Battjes, H. Bakkenes, T. Janssen, and A. R. van Dongeren. Shoaling of subharmonic gravity waves. *Journal of Geophysical Research: Oceans*, 109(C2), 2004.

J. A. Battjes. Surf similarity. In *Coastal Engineering 1974*, pages 466–480. 1975.

X. Bertin and M. Olabarrieta. Relevance of infragravity waves in a wave-dominated inlet. *Journal of Geophysical Research: Oceans*, 121(8):5418–5435, 2016.

X. Bertin, A. De Bakker, A. Van Dongeren, G. Coco, G. André, F. Ardhuin, P. Bonneton, F. Bouchette, B. Castelle, W. C. Crawford, et al. Infragravity waves: From driving mechanisms to impacts. *Earth-Science Reviews*, 177:774–799, 2018.

X. Bertin, D. Mendes, K. Martins, A. B. Fortunato, and L. Lavaud. The closure of a shallow tidal inlet promoted by infragravity waves. *Geophysical Research Letters*, 46(12):6804–6810, 2019.

J. Beyá, M. Álvarez, A. Gallardo, H. Hidalgo, C. Aguirre, J. Valdivia, C. Parra, L. Méndez, F. Contreras, P. Winckler, and M. Molina. *Atlas de Oleaje de Chile. Primera edición. Valparaíso, Chile, Escuela de Ingeniería Civil Oceánica - Universidad de Valparaíso.* 2016.

F. Biesel. Équations générales au second ordre de la houle irrégulière. *La Houille Blanche*, (3):372–376, 1952.

J. D. Bricker, I. Okabe, and A. Nakayama. Behavior of a small pulsed river plume in a strong tidal cross-flow in the Akashi Strait. *Environmental Fluid Mechanics*, 6(3):203–225, 2006.

M. Brocchini and T. Baldock. Recent advances in modeling swash zone dynamics: Influence of surf-swash interaction on nearshore hydrodynamics and morphodynamics. *Reviews of Geophysics*, 46(3), 2008.

B. L. Bruder and K. L. Brodie. Cirn quantitative coastal imaging toolbox. *SoftwareX*, 12:100582, 2020.

L. Burke, Y. Kura, K. Kassem, C. Revenga, M. Spalding, D. McAllister, and J. Caddy. *Coastal ecosystems*. World Resources Institute Washington, DC, 2001.

X. Cai, C. Ringler, and M. W. Rosegrant. *Modeling water resources management at the basin level: methodology and application to the Maipo River Basin*, volume 149. Intl Food Policy Res Inst, 2006.

Y. Chen, L. Chen, H. Zhang, and W. Gong. Effects of wave-current interaction on the Pearl River Estuary during Typhoon Hato. *Estuarine, Coastal and Shelf Science*, 228:106364, 2019.

S. Contardo and G. Symonds. Infragravity response to variable wave forcing in the nearshore. *Journal of Geophysical Research: Oceans*, 118(12):7095–7106, 2013.

R. Costanza. The ecological, economic, and social importance of the oceans. *Ecological economics*, 31(2): 199–213, 1999.

M. Delpey, F. Ardhuin, P. Otheguy, and A. Jouon. Effects of waves on coastal water dispersion in a small estuarine bay. *Journal of Geophysical Research: Oceans*, 119(1):70–86, 2014.

G. Dodet, X. Bertin, N. Bruneau, A. B. Fortunato, A. Nahon, and A. Roland. Wave-current interactions in a wave-dominated tidal inlet. *Journal of Geophysical Research: Oceans*, 118(3):1587–1605, 2013.

S. Elgar, T. Herbers, M. Okihiro, J. Oltman-Shay, and R. Guza. Observations of infragravity waves. *Journal of Geophysical Research: Oceans*, 97(C10):15573–15577, 1992.

K. L. Farnsworth and J. D. Milliman. Effects of climatic and anthropogenic change on small mountainous rivers: the Salinas River example. *Global and Planetary change*, 39(1-2):53–64, 2003.

F. Feddersen. Scaling surf zone turbulence. *Geophysical Research Letters*, 39(18), 2012.

F. Feddersen, M. Olabarrieta, R. Guza, D. Winters, B. Raubenheimer, and S. Elgar. Observations and modeling of a tidal inlet dye tracer plume. *Journal of Geophysical Research: Oceans*, 121(10):7819–7844, 2016.

F. Feddersen, A. B. Boehm, S. N. Giddings, X. Wu, and D. Liden. Modeling Untreated Wastewater Evolution and Swimmer Illness for Four Wastewater Infrastructure Scenarios in the San Diego-Tijuana (US/MX) Border Region. *GeoHealth*, 5(11):e2021GH000490, 2021.

R. P. Flores, P. A. Catalán, and M. C. Haller. Estimating surfzone wave transformation and wave setup from remote sensing data. *Coastal Engineering*, 114:244–252, 2016.

R. P. Flores, M. E. Williams, and A. R. Horner-Devine. River plume modulation by infragravity wave forcing. *Geophysical Research Letters*, 49(15):e2021GL097467, 2022.

R. D. Garreaud, C. Alvarez-Garreton, J. Barichivich, J. P. Boisier, D. Christie, M. Galleguillos, C. LeQuesne, J. McPhee, and M. Zambrano-Bigiarini. The 2010–2015 megadrought in central Chile: impacts on regional hydroclimate and vegetation. *Hydrology and Earth System Sciences*, 21(12):6307–6327, 2017.

R. D. Garreaud, J. P. Boisier, R. Rondanelli, A. Montecinos, H. H. Sepúlveda, and D. Veloso-Aguila. The central Chile mega drought (2010–2018): a climate dynamics perspective. *International Journal of Climatology*, 40(1):421–439, 2020.

M. A. Goñi, J. A. Hatten, R. A. Wheatcroft, and J. C. Borgeld. Particulate organic matter export by two contrasting small mountainous rivers from the Pacific Northwest, USA. *Journal of Geophysical Research: Biogeosciences*, 118(1):112–134, 2013.

S. B. Grant, J. H. Kim, B. H. Jones, S. A. Jenkins, J. Wasyl, and C. Cudaback. Surf zone entrainment, alongshore transport, and human health implications of pollution from tidal outlets. *Journal of Geophysical Research: Oceans*, 110(C10), 2005.

R. Guza and E. B. Thornton. Velocity moments in nearshore. *Journal of waterway, port, coastal, and ocean engineering*, 111(2):235–256, 1985.

R. D. Hetland. The effects of mixing and spreading on density in near-field river plumes. *Dynamics of Atmospheres and Oceans*, 49(1):37–53, 2010.

F. Hlawatsch and F. Auger. *Time-frequency analysis*. John Wiley & Sons, 2013.

A. R. Horner-Devine, R. D. Hetland, and D. G. MacDonald. Mixing and transport in coastal river plumes. *Annual Review of Fluid Mechanics*, 47:569–594, 2015.

J. G. Izett and K. Fennel. Estimating the cross-shelf export of riverine materials: Part 2. Estimates of global freshwater and nutrient export. *Global Biogeochemical Cycles*, 32(2):176–186, 2018.

T. Janssen, J. Battjes, and A. Van Dongeren. Long waves induced by short-wave groups over a sloping bottom. *Journal of Geophysical Research: Oceans*, 108(C8), 2003.

L. Jia, Y. Wen, S. Pan, J. T. Liu, and J. He. Wave–current interaction in a river and wave dominant estuary: A seasonal contrast. *Applied Ocean Research*, 52:151–166, 2015.

G. R. Jones, J. D. Nash, R. L. Doneker, and G. H. Jirka. Buoyant surface discharges into water bodies. I: Flow classification and prediction methodology. *Journal of Hydraulic Engineering*, 133(9):1010–1020, 2007.

S. Kastner, A. Horner-Devine, and J. Thomson. A conceptual model of a river plume in the surf zone. *Journal of Geophysical Research: Oceans*, 124(11):8060–8078, 2019.

S. Kastner, A. R. Horner-Devine, J. M. Thomson, and S. N. Giddings. Observations of River Plume Mixing in the Surf Zone. *Journal of Physical Oceanography*, 2022. doi: 10.1175/JPO-D-21-0286.1. URL `https://journals.ametsoc.org/view/journals/phoc/aop/JPO-D-21-0286.1/JPO-D-21-0286.1.xml`.

J. Lacaux, Y. Tourre, C. Vignolles, J. Ndione, and M. Lafaye. Classification of ponds from high-spatial resolution remote sensing: Application to Rift Valley fever epidemics in Senegal. *Remote Sensing of Environment*, 106(1):66–74, 2007.

J. M. Lilly and S. C. Olhede. Generalized Morse wavelets as a superfamily of analytic wavelets. *IEEE Transactions on Signal Processing*, 60(11):6036–6041, 2012.

C. J. Littles, C. A. Jackson, T. H. DeWitt, and M. C. Harwell. Linking people to coastal habitats: A meta-analysis of final ecosystem goods and services on the coast. *Ocean & coastal management*, 165:356–369, 2018.

M. S. Longuet-Higgins. Longshore currents generated by obliquely incident sea waves: 1. *Journal of geophysical research*, 75(33):6778–6789, 1970.

M. S. Longuet-Higgins and R. Stewart. Radiation stress and mass transport in gravity waves, with application to 'surf beats'. *Journal of Fluid Mechanics*, 13(4):481–504, 1962.

M. S. Longuet-Higgins and R. Stewart. Radiation stresses in water waves; a physical discussion, with applications. In *Deep sea research and oceanographic abstracts*, volume 11, pages 529–562. Elsevier, 1964.

M. L. Martínez, A. Intralawan, G. Vázquez, O. Pérez-Maqueo, P. Sutton, and R. Landgrave. The coasts of our world: Ecological, economic and social importance. *Ecological economics*, 63(2-3):254–272, 2007.

E. A. Martinez-Ríos, R. Bustamante-Bello, S. Navarro-Tuch, and H. Perez-Meana. Applications of the Generalized Morse Wavelets: A Review. *IEEE Access*, 2022.

I. Masotti, P. Aparicio-Rizzo, M. A. Yevenes, R. Garreaud, L. Belmar, and L. Farías. The influence of river discharge on nutrient export and phytoplankton biomass off the central chile coast (33–37 s): seasonal cycle and interannual variability. *Frontiers in Marine Science*, 5:423, 2018.

L. Melito, M. Postacchini, A. Sheremet, J. Calantoni, G. Zitti, G. Darvini, and M. Brocchini. Wave-current interactions and infragravity wave propagation at a microtidal inlet. In *Multidisciplinary Digital Publishing Institute Proceedings*, volume 2, page 628, 2018.

M. Miche. Mouvements ondulatoires de la mer en profondeur constante ou décroissante. *Annales de Ponts et Chaussées, 1944, pp (1) 26-78,(2) 270-292,(3) 369-406*, 1944.

J. D. Milliman and J. P. Syvitski. Geomorphic/tectonic control of sediment discharge to the ocean: the importance of small mountainous rivers. *The Journal of Geology*, 100(5):525–544, 1992.

S. Moghimi, H. T. Özkan-Haller, Ç. Akan, and J. T. Jurisa. Mechanistic analysis of the wave-current interaction in the plume region of a partially mixed tidal inlet. *Ocean Modelling*, 134:110–126, 2019.

T. Moura and T. Baldock. Remote sensing of the correlation between breakpoint oscillations and infragravity waves in the surf and swash zone. *Journal of Geophysical Research: Oceans*, 122(4):3106–3122, 2017.

R. B. Nairn. Prediction of cross-shore sediment transport and beach profiles evolution. 1990.

M. Olabarrieta, J. C. Warner, and N. Kumar. Wave-current interaction in Willapa Bay. *Journal of Geophysical Research: Oceans*, 116(C12), 2011.

M. Olabarrieta, W. R. Geyer, and N. Kumar. The role of morphology and wave-current interaction at tidal inlets: An idealized modeling analysis. *Journal of Geophysical Research: Oceans*, 119(12):8818–8837, 2014.

A. Osadchiev, R. Sedakov, and A. Barymova. Response of a small river plume on wind forcing. *Frontiers in Marine Science*, 2021.

B. A. O'Connor, S. Pan, J. Nicholson, N. MacDonald, and D. A. Huntley. A 2d model of waves and undertow in the surf zone. In *Coastal Engineering 1998*, pages 286–296. 1999.

M. D. Peña-Guerrero, A. Nauditt, C. Muñoz-Robles, L. Ribbe, and F. Meza. Drought impacts on water quality and potential implications for agricultural production in the Maipo River Basin, Central Chile. *Hydrological Sciences Journal*, 65(6):1005–1021, 2020.

D. H. Peregrine. Interaction of water waves and currents. *Advances in applied mechanics*, 16:9–117, 1976.

M. R. Poe, K. C. Norman, and P. S. Levin. Cultural dimensions of socioecological systems: key connections and guiding principles for conservation in coastal environments. *Conservation Letters*, 7(3):166–175, 2014.

A. Pomeroy, R. Lowe, G. Symonds, A. Van Dongeren, and C. Moore. The dynamics of infragravity wave transformation over a fringing reef. *Journal of Geophysical Research: Oceans*, 117(C11), 2012.

M. Pritchard and D. A. Huntley. A simplified energy and mixing budget for a small river plume discharge. *Journal of Geophysical Research: Oceans*, 111(C3), 2006.

W. V. Reid and K. R. Miller. *Keeping options alive*. 1989.

A. Reniers, M. Groenewegen, K. Ewans, S. Masterton, G. Stelling, and J. Meek. Estimation of infragravity waves at intermediate water depth. *Coastal Engineering*, 57(1):52–61, 2010.

A. J. Reniers, R. Naporowski, M. F. Tissier, M. A. de Schipper, G. Akrish, and D. P. Rijnsdorp. North Sea infragravity wave observations. *Journal of Marine Science and Engineering*, 9(2):141, 2021.

A. R. Rodriguez, S. N. Giddings, and N. Kumar. Impacts of nearshore wave-current interaction on transport and mixing of small-scale buoyant plumes. *Geophysical Research Letters*, 45(16):8379–8389, 2018.

M. W. Rosegrant, C. Ringler, D. C. McKinney, X. Cai, A. Keller, and G. Donoso. Integrated economic-hydrologic water modeling at the basin scale: The Maipo River basin. *Agricultural Economics*, 24(1): 33–46, 2000.

H. A. Schäffer. Infragravity waves induced by short-wave groups. *Journal of Fluid Mechanics*, 247:551–588, 1993.

C. Small and R. J. Nicholls. A global analysis of human settlement in coastal zones. *Journal of coastal research*, pages 584–599, 2003.

I. A. Svendsen. Mass flux and undertow in a surf zone. *Coastal engineering*, 8(4):347–365, 1984.

G. Symonds, D. A. Huntley, and A. J. Bowen. Two-dimensional surf beat: Long wave generation by a time-varying breakpoint. *Journal of Geophysical Research: Oceans*, 87(C1):492–498, 1982.

J. P. Syvitski, S. D. Peckham, R. Hilberman, and T. Mulder. Predicting the terrestrial flux of sediment to the global ocean: a planetary perspective. *Sedimentary Geology*, 162(1-2):5–24, 2003.

G. Thomas. Wave-current interactions: an experimental and numerical study. part 1. Linear waves. *Journal of Fluid Mechanics*, 110:457–474, 1981.

J. A. Warrick and J. D. Milliman. Hyperpycnal sediment discharge from semiarid southern California rivers: Implications for coastal sediment budgets. *Geology*, 31(9):781–784, 2003.

J. A. Warrick, P. M. DiGiacomo, S. B. Weisberg, N. P. Nezlin, M. Mengel, B. H. Jones, J. C. Ohlmann, L. Washburn, E. J. Terrill, and K. L. Farnsworth. River plume patterns and dynamics within the Southern California Bight. *Continental Shelf Research*, 27(19):2427–2448, 2007.

M. E. Williams and M. T. Stacey. Tidally discontinuous ocean forcing in bar-built estuaries: The interaction of tides, infragravity motions, and frictional control. *Journal of Geophysical Research: Oceans*, 121(1): 571–585, 2016.

S. H. Wong, S. G. Monismith, and A. B. Boehm. Simple estimate of entrainment rate of pollutants from a coastal discharge into the surf zone. *Environmental Science & Technology*, 47(20):11554–11561, 2013.

S. Zippel and J. Thomson. Wave breaking and turbulence at a tidal inlet. *Journal of Geophysical Research: Oceans*, 120(2):1016–1031, 2015.